THE PENNSYLVANIA STATE UNIVERSITY
SCHREYER HONORS COLLEGE

DEPARTMENT OF BIOMEDICAL ENGINEERING

ENGINEERING BIOMIMETIC ANTICANCER THERAPIES

MATTHEW ARONSON
SPRING 2020

A thesis
submitted in partial fulfillment
of the requirements
for a baccalaureate degree
in Biomedical Engineering
with honors in Biomedical Engineering

Reviewed and approved* by the following:

Scott H. Medina
Assistant Professor of Biomedical Engineering
Thesis Supervisor

Jian Yang
Professor of Biomedical Engineering
Lloyd & Dorothy Foehr Huck Chair in Regenerative Engineering
Honors Adviser

Deborah F. Kelly
Professor of Biomedical Engineering
Director, Center for Structural Oncology
Thesis Reader

* Signatures are on file in the Schreyer Honors College.

ABSTRACT

Antimicrobial peptides (AMPs) are short, cationic amphiphiles, ubiquitous in nature as a part of organisms' immune systems, that preferentially kill bacterial pathogens through folding-dependent membrane disruption. Briefly, this antibacterial activity is initiated by electrostatic interactions between the cationic peptide and anionic bacterial surface, followed by subsequent interpolation of the sequence into the hydrophobic cell envelope of the cell. Interestingly, bacteria and cancer cells share a common trait – both possess an electronegative exterior that distinguishes them from healthy mammalian counterparts. This opens opportunities to re-design antimicrobial peptides (AMPs) into anticancer peptides (ACPs). To test this assertion, I investigate the ability of a pathogen-specific AMP named MAD1, originally designed to kill bacterial tuberculosis, to potentiate the lytic destruction of drug-resistant cancers and synergistically enhance the efficacy of chemotherapeutics. Structure-activity relationships (SAR)-driven de novo design reveals spatial sequestration of amphiphilic regions increases ACP potency, but at the cost of specificity. Biophysical and biochemical studies demonstrate that MAD1 binds to the outer membrane of cancer cells to rapidly form pore-like supramolecular assemblies, leading to rapid cell death through both lytic and apoptotic mechanisms. This diverse anticancer activity enables MAD1 to synergize broadly with chemotherapeutics, particularly against drug-resistant ovarian cancer cells and patient-derived tumor models, leading to remarkable combinatorial potency.

Yet, despite the attractive therapeutic properties of synergistic ACPs, like MAD1, their successful translation into clinical practice has gone unrealized due to the poor bioavailability, serum instability and, most importantly, severe hemolytic toxicity of membranolytic sequences. Therefore, in a parallel project, I exploit the membrane-specific interactions of ACPs to prepare a

new class of peptide-lipid particle, I term a lipopeptisome (LP). This design sequesters loaded ACPs within a lipid lamellar corona to avoid contact with red blood cells and healthy tissues, while affording potent lytic destruction of cancer cells following LP-membrane fusion. Biophysical studies show ACPs rapidly fold at, and integrate into, liposomal membranes to form stable LPs with high loading efficiencies (>80%). Rational design of the particles to possess lipid combinations mimicking that of the aberrant cancer cell outer leaflet allows LPs to rapidly fuse with tumor cell membranes and afford localized assembly of loaded ACPs within the bilayer. This leads to preferential fusolytic killing of cancer cells with minimal collateral toxicity towards non-cancerous cells and erythrocytes, thereby imparting clinically relevant therapeutic indices to otherwise toxic ACPs.

Together, I show cancer-specific ACPs can be rationally engineered using nature's AMP tool-box as templates, demonstrate the potential of this strategy to open a wealth of synthetic biotherapies that offer new, combinatorial opportunities against drug resistant tumors, and offer the Lipopeptisomes design as a novel drug delivery platform to improve ACP potency and specificity. Future studies will combine this delivery technology with bioinspired ACPs to develop targeted, combinatorial therapies that are effective against multidrug resistant cancers.

TABLE OF CONTENTS

LIST OF FIGURES

LIST OF TABLES

ACKNOWLEDGEMENTS

I thank Dr. Scott H. Medina in the Department of Biomedical Engineering at Penn State University for his support as an honors thesis advisor, research advisor, and mentor. Additionally, I thank the rest of the Medina Lab Group, specifically Andrew Simonson, Janna Sloand, and Atip Lawanprasert for their support, training, and scientific opinion throughout my undergraduate research experience. I also thank my friends and family for their support and encouragement.

I acknowledge and thank Lindsey M. Orchard (Department of Biochemistry and Molecular Biology, Penn State University, University Park, PA) and Manuel Llinás (Departments of Biochemistry and Molecular Biology, Chemistry, and Huck Center for Malaria Research, Penn State University, University Park PA) for their contributions to the published work titled "Lipopeptisomes: Anticancer Peptide-Assembled Particles for Fusolytic Oncotherapy." I also thank Erika S. Dahl and Katherine M. Aird (Department of Cellular & Molecular Physiology, Penn State College of Medicine, Hershey, PA), Rose A. Gogal and Adam B. Glick (Department of Veterinary and Biomedical Sciences, Penn State University, University Park, PA), and Jacob A. Halle (Department of Biomedical Engineering, Penn State University, University Park, PA) for their contributions to the published work titled "Re-engineering Antimicrobial Peptides into Oncolytics Targeting Drug-Resistant Ovarian Cancers."

I also thank the laboratory of Dr. Joel Schneider at the National Cancer Institute for providing cancer cell lines. I also thank Dr. Matthew Taylor (Penn State University, College of Medicine, Hershey, PA) for donating the NL20 cell line. I acknowledge and thank the laboratories of Dr. Zissis Chroneos (Penn State University, College of Medicine, Hershey, PA), Dr. Pak Kin Wong (Penn State University, PA), and Dr. Kenneth Keiler (Penn State University, PA) for sharing

the bacterial strains employed in these studies. I also recognize and thank the Penn State Microscopy and Cytometry Facility – University Park, PA for assistance with confocal microscopy and cryo-TEM sample prep, imaging and analysis. I also acknowledge the Penn State X-Ray Crystallography Facility – University Park, PA and Penn State Materials Characterization Laboratory – University Park, PA for use of the CD spectrophotometer and dynamic light scattering instrumentation, respectively.

Funding for this research was provided by the Penn State Institute of Energy and the Environment Human Health and the Environment Seed Grant (S.H.M.), Laboratory Startup Funds from the Pennsylvania State University (S.H.M.), NIH:R00CA194309 (K.M.A.), NIH:F31CA236372 (E.S.D.), Penn State College of Engineering Grant (M.R.A.), Penn State Schreyer Honors College Independent Research Grant (M.R.A.), Penn State Student Engagement Network Grant (M.R.A.), and Penn State Graduate Research Fellowship (A.W.S.). The findings and conclusions in this thesis do not necessarily reflect the views of the funding agencies.

Chapter 1

Introduction

Cancer is a significant global health concern, and is the second leading cause of death in the United States.[1] In 2019, it was estimated that there were 1,762,450 new cases of cancer taking the lives of over 600,000 individuals—equating to approximately 1,700 deaths per day.[2–4] There are many factors that impact carcinogenesis. Certain compounds, known as carcinogens, increase the probability of mutating healthy cell genetic information and subsequently causing cancer, other factors such as environmental exposures, natural hormone levels, and life-long nutrition impact this as well. With all the research that has been conducted up to this point, there are still a strong presence of cancer in society dictating a clear need for improved oncotherapies.

Current Limitations in Cancer Therapies

Multidrug resistance (MDR) is a phenomenon defined by a cancer's ability to resist the cytotoxic effects of chemotherapeutics by methods such as drug inactivation, therapeutic target alteration, drug efflux, DNA damage repair, cell death inhibition, and epithelial-mesenchymal transition.[5–7] Cancer has the propensity to acquire these resistance mechanisms due to high rates of replication, which increase the likelihood of cancer promoting mutations. One goal of cancer therapy is to specifically target the tumor cells, while avoiding toxicity to heathy counterparts. Of the numerous targeting mechanisms for cancer therapeutics, one example is targeting highly proliferative cells with drugs such as DNA alkylating agents, antimetabolites, intercalating agents, and mitotic inhibitors.[8] Other drugs focus on inhibiting specific pathways such as the MDR gene where the transmembrane protein P-glycoprotein (P-gp) is overexpressed. In this situation, once drugs are internalized via diffusion or endocytosis into the cancer cell, they are

immediately effluxed by P-gp and have no opportunity to kill the cell. Similar to the overexpression of P-gp, other proteins such as topoisomerase II and p53 can also be mutated in MDR leading to the inability of cell induced apoptosis when faced with DNA damage. The increased prevalence of MDR is becoming a great concern as we run out of effective chemotherapeutics to treat cancer.

In addition to limitations of treatment due to MDR, there are prior factors that inhibit chemotherapeutic efficacy such as degradation and off target effects. The first problem with most anticancer agents is their propensity to bind to serum proteases and globular proteins, such as human serum albumin and transferrin, in the blood.[9–12] When administered intravenously, this not only prevents the drug from reaching its target, but certain proteases will begin to degrade the compounds through bond cleavage causing the body to excrete the compound readily. The second large limitation of chemotherapeutic utility are the multitude of side effects that normally incur. Even when a drug is classified as specific or targeting, there are still off target toxicities due to the distinction between specific and exclusive targeting.[12,13] As an example, Adriamycin, or doxorubicin, is usually prescribed for chemotherapeutic treatment of solid tumors and hematologic malignancies.[14] Unfortunately, these treatments have both acute and chronic implications on healthy tissues. In particular, doxorubicin-mediated cardiotoxicity induces changes in the heart structure, congestive heart failure, and results in irreversible damage that often requires a heart transplant.[14,15] Long term effects of doxorubicin treatment include gastrointestinal toxicity, asymptomatic systolic disfunction, and neurological disorders after 5 years of treatments.[16,17] Cisplatin, or *cis*-diamminedichloroplatinum(II), is the most commonly administered chemotherapy for solid tumor treatment in numerous biological systems such as reproductive, gastrointestinal, and pulmonary tracts. Among the common side effects of this treatment, gastrointestinal symptoms such as nausea and vomiting are almost always seen, as well as fevers, hyposthenia, and alteration in the liver; some of the less common but more severe side effects are neurotoxicity, nephrotoxicity, and ototoxicity.[18–22] Doxorubicin and Cisplatin are just two examples of chemotherapies that exhibit dose-dependent side effects, which will continue to act as severe limitations on treating cancer diagnoses.

The Emergence of Anticancer Peptides

Chemotherapeutic resistance is the first limitation addressed as it is a frequent cause of treatment failure in oncology, often preceding disease relapse and patient death.[23,24] It is now common practice to select combinatorial cocktails of drugs with different mechanisms of action to prevent the emergence of resistant cell sub-populations. These regimens almost exclusively employ small molecule inhibitors that act on intracellular biochemical pathways,[25,26] while compounds that target and disrupt the membranes of cancer cells are comparatively underexplored.[27,28] Yet, there is accelerating clinical interest in adding tumor lytic agents to combinatorial therapies due to their ability to kill cancer cells through physical mechanisms that are not shared by conventional drugs.[29–31]

Anticancer peptides (ACPs) are one such class of potential therapeutics that exert their action by preferentially intercalating into and disrupting the plasma and mitochondrial membranes of cancer cells.[30,32] These membrane-destabilizing effects can promote the intracellular diffusion and passive transport of otherwise poorly permeable small molecule drugs and biologics.[33,34] More importantly, the rapid and non-stereospecific mechanisms of ACPs have led to the conclusion that evolutionary resistance towards these agents is probabilistically low.[30,35] Taken together, these attributes suggest that ACPs could have significant potential to advance combinatorial strategies in precision medicine if properly exploited.

Mechanisms of Anticancer Peptides

The precise mechanism of ACP cell cytotoxicity is largely classified into two main categories: plasma membrane disruption[36] and activation of apoptotic pathways (**Fig. 1**[37]).[38–40] More specifically, the method of membrane destabilization can be further delineated into three groups.[12,36] (1) Barrel-stave pores (**Fig. 1a**) where the ACP disrupts the cell membrane by inserting perpendicularly to the surface, followed by insertion of the peptide's hydrophobic surface into the lipophilic membrane into the acyl fatty acid chains

of the lipids. (2) Toroidal pores (**Fig. 1b**) insert into the membrane while remaining in continuous contact with both the head groups and acyl side chains to form pores via induced cell curvature. (3) The carpet and detergent-like mechanism (**Fig. 1c**) is induced when high concentrations of peptide interact with the head groups of the cell membrane invoking high amounts of curvature strain—this leads to membrane blebbing and the formation of small micelles of membrane and intracellular debris. When it is not possible to discretely determine the mechanism through which cell death is occurring, the Shai-Huang-Matsuzaki (SHM) model is used since claims there is no single mechanism responsible for pore formation and cell death.[36,41] According to SHM, most events begin with an interaction close to that of the carpet mechanism where a low concentration of peptides reside either on the outer leaflet of the plasma membrane with hydrophobic residues inserted in the membrane and hydrophilic residues exposed to the aqueous environment, or interpolated vertically in the membrane. Once in the membrane, the peptides either move around fluidly in the lipid rafts or anchor to transmembrane proteins that reduce their movement.[42,43] It is not until a certain threshold concentration is reached that the peptides self-assemble,

create high curvature strain or membrane stress, and interpolate into the membrane to either form pores or create micelles. Further, this may induce molecular electroporation (**Fig. 1d**) due to membrane depolarization, or a sinking raft (**Fig. 1e**) when the membrane begins to collapse on itself. All of the aforementioned methods lead to cell death via immediate cell lysis or stress induced apoptosis.[12,36]

It is also worth noting that if ACPs pass through the plasma membrane or enter the cytoplasm via pores, intracellular disruption may occur inducing apoptosis through an intrinsic caspase cascade following mitochondrial membrane disruption or nuclear degradation.

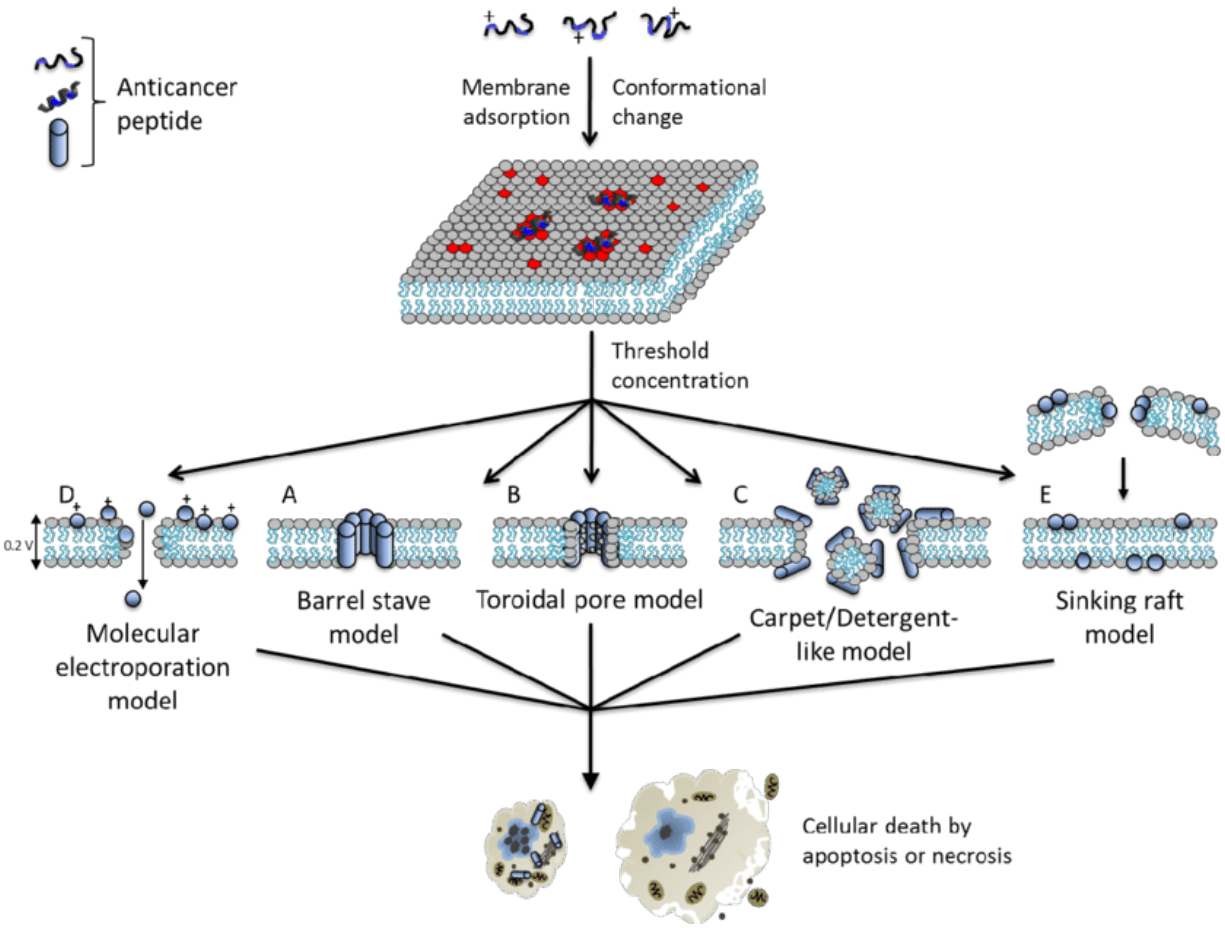

Figure 1. Proposed Mechanisms for Membrane Disruption. (**A**) Barrel-stave pore where peptide interacts with membrane lipid acyl fatty acids. (**B**) Toroidal pores where peptide interacts with membrane lipid phosphate groups. (**C**) Carpet or detergent-like mechanism where peptide concentration disrupts membrane and forms small blebs or micelles. (**D**) Pore formation leads to the depolarization of the membrane due to ion exchange through the pores. (**E**) Sinking raft model where the membrane begins turning inside out due to the collapsing of pores. This figure is retrieved from Ketil André Camilio[37], with modified figure description.

Engineering Novel ACPs for Chemotherapy Synergy

ACP discovery campaigns are important for locating new sequences that potentiate the ability to circumvent many of the previously described limitations of cancer therapy. Sadly, they are normally constrained by the need for large empirical screens of complex natural product mixtures.[44–46] These methods are costly, laborious and hindered by extensive med-chem optimization of lead candidates. As an alternative strategy, here we explore the potential to directly re-purpose nature's toolbox of antimicrobial peptides to

produce a robust ACP discovery pipeline. Antimicrobial peptides (AMPs) are a diverse family of natural, membrane-active antimicrobials that have evolved as vital weapons in the arms-race against pathogenic bacteria for a variety of lifeforms, from microorganisms to mammals (e.g. defensins).[47,48] The bactericidal activity of cationic AMPs is initiated by electrostatic interactions with the highly anionic glycocalyx of bacteria, causing peptide-glycan binding that precedes interpolation into the cell envelope and self-assembly to form lytic pores.[49,50] Similar to bacteria, cancer cells possess an increased electronegative surface charge compared to non-cancerous cells due to aberrant glycosylation and metabolism processes that yield sialic acid rich surface polysaccharides and overexpression of phosphatidylserine on the outer leaflet, respectively.[51–54] Electrostatic association of cationic ACPs with the electronegative cancer cell surface drives the folding of these sequences into α-helical, β-sheet, loop, extended helical, cyclic, and mixed structure bioactive conformations.[30,38,39,41,55] These coincident phenotypes of bacteria and tumor cells encourages the use of AMPs for anticancer applications,[30] and suggests we may be able to directly employ AMP templates, which have already been pre-optimized by evolution, to rationally design new ACPs. Here we test this assertion by investigating the ability and mechanism of MAD1, a pathogen-specific AMP with potent activity towards bacterial tuberculosis, to kill drug-resistant cancers and synergistically enhance the potency of chemotherapeutics (**Fig. 2**).

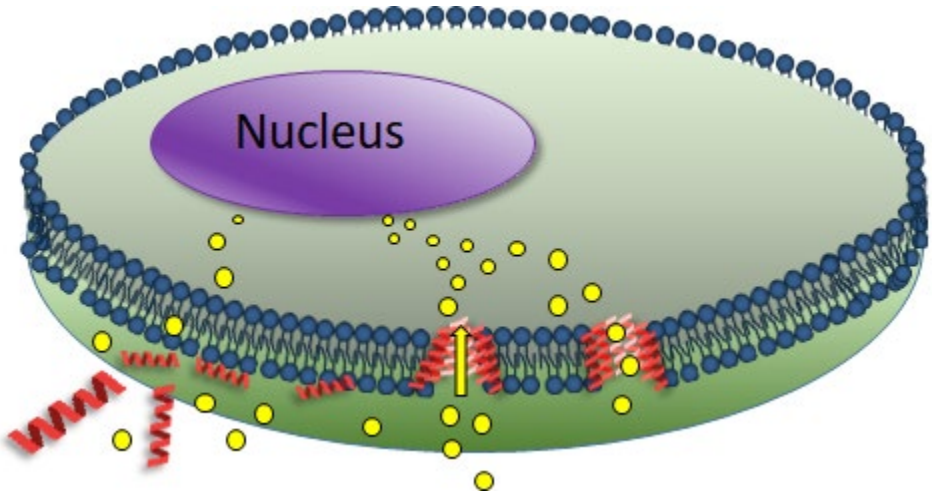

Figure 2. Illustration of the proposed synergistic co-administration of MAD1 peptide (red) with a clinically approved chemotherapeutic (yellow). Here, the peptide self-assembles to form pores, but due to the low concentration of peptide, the pores

do not cause cell lysis. Instead, they facilitate the chemotherapeutic movement across the membrane to enter the cytoplasm and induce apoptosis.

Enhancing the Delivery of ACPs

Yet, despite their significant therapeutic potential, the clinical translation of ACPs has been limited by the same limitations of other previously discovered chemotherapeutics. ACPs undergo a rapid systemic clearance in the circulatory system, and poorly distribute to tumor tissue.[12,28] Peptides are especially susceptible to protease degradation and serum binding due to the biological functions in the body; proteins inherently bind to these types of biomacromolecules catabolize the peptide bonds to release amino acids for protein synthesis.[36,55] This necessitates large doses of ACPs to be administered in vivo, often at or above tolerated concentrations, to achieve antitumor responses.[28,35,53] The resulting hemolysis and destruction of healthy cells at these high concentrations ultimately leads to severe dose-limiting toxicities. This off-target activity of ACPs is largely due to the small, but still significant, presence of negatively charged lipids, such as phosphatidylethanolamine, on the outer membrane of healthy mammalian tissues and red blood cells.[56–58] Although not as abundant as on the surfaces of cancer cells,[59–61] this modest anionic charge is sufficient to potentiate the binding of ACPs and cause damage to non-cancerous cell membranes at high peptide concentrations. Thus, delivery systems that can localize ACPs to tumor tissue and preferentially integrate the lytic cargo into cancer cell membranes, while evading off-target toxicity towards red blood cells and healthy tissues, represent an attractive strategy to improve the clinical utility of these potentially potent and efficacious anticancer drug candidates.

Lipopeptisome Design

Here, I leverage the membrane-specific interactions of ACPs to prepare a new class of peptide-loaded lipid particle, which I term a lipopeptisome (LP) (**Fig. 3**). This design pre-folds loaded ACPs into

their bioactive lytic state as an α-helix, while sequestering the peptide cargo from proteases and red blood cells in the systemic circulation. Fusion of LPs with cancer cell membranes leads to direct assimilation of loaded ACPs into the lipid bilayer, where subsequent peptide self-assembly forms lytic pores. This strategy allows LPs to elicit preferential fusolytic killing of cancer cells while being remarkably biocompatible towards healthy cells and erythrocytes; thus affording clinically viable therapeutic indices to otherwise highly toxic ACPs. Hence, LPs may serve as a simple, effective delivery platform to improve the efficacy and safety profile of oncolytic molecules challenged by poor stability and off-target side effects. First, particles will be formed mimicking the natural lipid composition of a cancer cell. Next, three anticancer peptide sequences from literature—A4K14-citropin 1.1,[62] Halictine 2/11,[63] and Lasioglossin III[63]—will be tested due to their low specificity but high toxicity. The sequences will be tested alone against cancer cells, healthy cells, and erythrocytes, and subsequently combined with LPs and put through the same experiments to determine the therapeutic window of the ACP LP combination. Experiments such as circular dichroism and dynamic light scattering will be used to determine the structure of the peptides and size and integrity of the particles. Then confocal microscopy will be utilized with co-labeled LPs to investigate the mechanism of LP membrane fusion and activity.

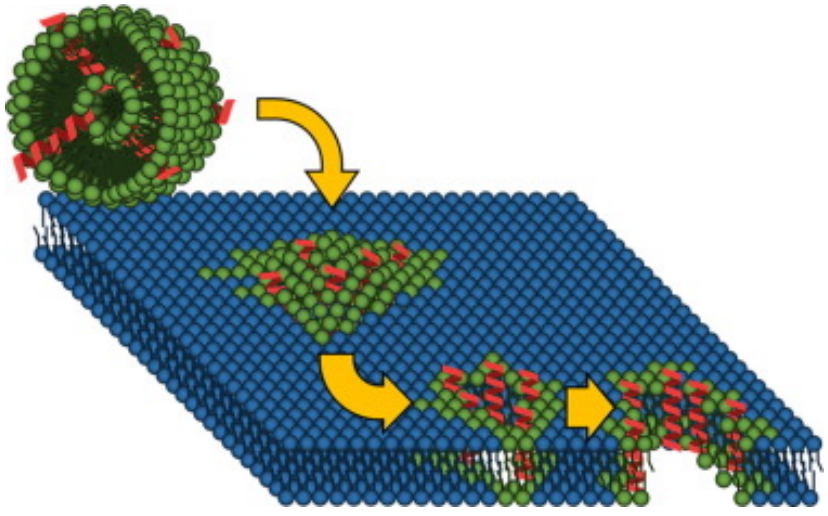

Figure 3. Schematic illustration of LP composition and proposed fusolytic anticancer mechanism. Particles are formed via integration of ACPs (red) within a liposomal carrier (green) which possesses a similar lipid composition to that of the cancer cell membrane (shown in blue for clarity). The resulting fusion of LPs with cancer cell membranes leads to direct assimilation of loaded ACPs within the lipid bilayer. Subsequent peptide self-assembly forms lytic pores that leads to preferential tumor cell lysis.

Chapter 2
Materials & Methods

Materials

1,2-ethanedithiol and diethyl ether were purchased from Acros Organics. 1,3-bis[tris(hydroxymethyl)methylamino]propane (BTP), piperidine, dimethyl sulfoxide spectrophotometer grade (DMSO), and thioanisole were purchased from Alfa Aesar. Vascular Cell Basal Medium, Rh VEGF, rg EGF, rg FGF basic, rg IGF-1, L-glutamine, heparin sulfate, hydrocortisone hemisuccinate, FBS, and ascorbic acid were purchased from ATCC. 1-palmitoyl-2-oleoyl-sn-glycero-3-phosphocholine (POPC), 1-palmitoyl-2-oleoyl-sn-glycero-3-phospho-L-serine (POPS), 1,2-dioleoyl-sn-glycero-3-phosphoethanolamine (DOPE), and 1,2-dioleoyl-sn-glycero-3-phosphoethanolamine-N-(lissamine rhodamine B sulfonyl) ($PE_{rhodamine}$) were purchased from Avanti Polar Lipids. Sodium fluoride and sodium hydroxide were purchased from BDH. FITC Annexin V Apoptosis Detection Kit with PI was purchased from BioLegend. 0.2μm nitrocellulose membrane were purchased from Bio-Rad. Cleaved Caspase-3 Rabbit Ab and β-Actin (8H10D10) Mouse mAb were purchased from Cell Signaling Technology. Fmoc-protected amino acids, oxyma, and Rink Amide ProTide Resin were purchased from CEM. Paraformaldehyde was purchased from Chem Cruz. 3-(4,5-Dimethyl-2-thiazolyl)-2,5-diphenyl-2H-tetrazolium bromide (MTT), Fmoc-protected amino acids, N,N'-diisopropylcarbodiimide (DIC), O-(7-Azabenzotriazol-1-yl)-N,N,N',N'-tetramethyluronium hexafluorophosphate (HATU), N,N-dimethylformamide (DMF), 5(6) carboxyfluorescein, and Paclitaxel were purchased from Chem-Impex International, Inc. RPMI-1640, M199, trypsin and EDTA solution, Antibiotic-Antimycotic Solution, ultra-low attachment (ULA) plates, and 1x phosphate buffered saline (PBS) were purchased from Corning. Calcium and magnesium free Dulbecco's phosphate-buffered saline (DPBS) was purchased from Gibco. Fetal bovine serum was purchased from HyClone. Hoechst 33342 trihydrochloride trihydrate dye was

purchased from Invitrogen. Goat anti-mouse IgG (LC Specific) and Peroxidase AffiniPure Goat Anti-Rabbit IgG (H+L) were purchased from Jackson ImmunoResearch. Glycerol, tween 80, oadc supplement, MEM non-essential amino acid solution, D-(+)-Glucose, Insulin (Recombinant human), Transferrin Apo-(human plasma), hydrocortisone, OmniPur® Tween® 20 (Polyoxyethylene (20) Monolaurate), and sodium bicarbonate were purchased from Millipore-Sigma. N,N-Diisopropylethlamine (DIEA) and Doxorubicin HCl were purchased from Oakwood. 5% Blotto Immunoanalytical Grade (Non-Fat Dry Milk) was purchased from Rockland Immunochemicals. Cisplatin was purchased from Selleck Chemical S1166. MCDB-105, EmbryoMax 0.1% gelatin solution, Triton X-100, potassium chloride (KCl), and FCCP (2-[2-[4-(trifluoromethoxy)phenyl]hydrazinylidene]-propanedinitrile) were purchased from Sigma-Aldrich. Cisplatin was purchased from Tocris Bioscience. Biotech CE dialysis tubing MWCO: 300kDa, Ultrapure Low Melting Point Agarose, Lysogeny broth, Mueller Hinton broth, 7H9 media, Nunc Lab-Tek Chambered Coverglass, sodium chloride (NaCl), hydrochloric acid (HCl), acetonitrile, trifluoroacetic acid (TFA), dichloromethane, dimethyl sulfoxide cell culture grade (DMSO), NHS-Fluorescein, 3500 MWCO Slide-A-Lyzer Dialysis Cassettes, Pierce ECL Western Blotting Substrate, SuperSignal West Dura Extended Duration Substrate, and formic acid LC/MS grade were purchased from ThermoFisher Scientific. Anisole was purchased from Tokyo Chemical Industry. F12 media, L-glutamine, tris, gentamycin, sodium fluoride, sodium hydroxide, sodium phosphate monobasic, and sodium phosphate dibasic were purchased from VWR.

A549, HeLa, OVCAR-3, T24, and NCI/ADR-RES cells were kindly provided by the laboratory of Dr. Joel P. Schneider (NCI, Frederick, MD). NL20 cell line was generously gifted by the laboratory of Dr. Matthew Taylor (Penn State University, College of Medicine, PA). *Pseudomonas aeruginosa*, *Escherichia coli*, *Bacillus subtilis*, methicillin-sensitive *Staphylococcus aureus*, methicillin-resistant *Staphylococcus aureus*, and *Mycobacterium tuberculosis* bacterial strains were generous gifts from the laboratories of Dr. Zissis Chroneos (Penn State, College of Medicine, Hershey, PA), Dr. Pak Kin Wong (Penn State,

Biomedical Engineering, University Park, PA) and Dr. Kenneth Keiler (Penn State, Biochemistry and Molecular Biology, University Park, PA).

Analytical LCMS solvents were composed as follows: solvent A is 0.1% formic acid in water and solvent B is 9:1 acetonitrile and water with 0.1% formic acid. Preparative HPLC solvents consisted of solvent A (0.1% TFA in water) and solvent B (9:1 acetonitrile and water with 0.1% TFA).

Peptide Synthesis

Synthesis and Cleavage

Peptide synthesis was carried out via Fmoc-based solid-phase peptide synthesis with Oxyma/N,N'-Diisopropylcarbodiimide (DIC) activation on Rink Amide ProTide resin using a Liberty Blue Automated Microwave Peptide Synthesizer (CEM, Matthews, NC). Cleavage from the resin and side-chain deprotection was performed simultaneously using a trifluoroacetic acid:thioanisole:1,2-ethanedithiol:anisole (90:5:3:2) solution stirred under argon for 2 hours for peptide sequences Citropin, Halictine, and Lasioglossin, and 3 hours for peptide sequences MAD1, DAP1, and DAP2. Cold diethyl ether was used to precipitate the crude peptide. After centrifugation at 5,000 rpm for 5 min. to collect the solids, the diethyl ether was decanted, and sample lyophilized overnight to remove trace amounts of organic solvent. Peptides were purified by reverse-phase HPLC (Shimadzu, Columbia, MD) equipped with a Phenomenex Semi-Prep Luna C18(2) column (Torrance, CA).

Purification

A linear gradient of 0-50% solvent B over 50 min. was used to purify the Citropin peptide. A gradient of 0 – 20% solvent B over 10 min., followed by 20 – 44% solvent B over an additional 24 min.,

was used to purify Halictine. Purification of Lasioglossin was performed using a linear gradient of 0 – 14% solvent B over 7 min., followed by 14 – 45% solvent B over an additional 31 min. For MAD1 peptide purification, a linear gradient of 0 – 25% solvent B over 25 min. was followed by a linear gradient of 25 – 45% solvent B over 40 min was used. For DAP1 peptide purification, a linear gradient of 0 – 42% solvent B over 38 min. was used. For DAP2 peptide purification, a linear gradient of 0 – 10% solvent B was used over 10 min. followed by a linear gradient of 10 – 25% solvent B over 30 min was used. All peptides were lyophilized and pure product collected for verification by analytical LC-MS ESI (+).

Fluorescently Labeling

Fluorescently-labeled Lasioglossin was prepared by reacting the N-terminal amine of the peptide on resin with 5(6)-carboxyfluorescein (2 eq.), HATU (1.9 eq.), and N,N-diisopropylethylamine (DIEA, 6 eq.) overnight while shaking at room temperature. Reaction completion was verified using the Ninhydrin Test to detect free amines.[64] Normal cleavage and purification protocols were followed as described above. To purify the labeled Lasioglossin peptide, a linear gradient of 0 – 32% solvent B over 16 min., followed by 32 – 45% solvent B for an additional 13 min., was used.

MAD1 was fluorescently labeled with NHS-Fluorescein (5/6-carboxyfluorescein succinimidyl ester) by combining peptide on resin with 2 equivalents of NHS-Fluorescein and 4 equivalents of diisopropylethalamine and allowed to shake at room temperature for 4 hours. Reaction completion was again checked using the Ninhydrin Test to detect free amines.[64] Cleavage and purification were completed according to previous protocols. Purification was conducted by first using a linear gradient of 0 – 12% solvent B over 6 min., followed by 12 – 32% solvent B over 20 min., and finally 32 – 38% solvent B over 12 min. Final characterization of both labeled sequences was completed on HPLC chromatograms and mass spectroscopy with ESI (+).

Particle Formulation

Liposome Formulation

Liposomes were formed using extrusion techniques as previously described.[12,65] Healthy liposomal mimicking membranes were prepared with 72:23:5 phosphatidylcholine (POPC): phosphatidylethanolamine (DOPE): phosphatidylserine (POPS) lipids. Cancer liposomal membranes were prepared with 45:24:30 POPC:DOPE:POPS. Lipopeptisomes were prepared with 1:1 photsphatidylcholine: phosphatidylserine. Liposomes were prepared by first combining the lipids in chloroform, followed by evaporation of the solvent under a stream of argon. The lipid film was then lyophilized overnight to dry completely, before rehydration with 2× concentrated liposome buffer (300mM BTP, 100mM NaF, and pH 7.4). The solution was then subjected to 8 freeze/thaw cycles in liquid nitrogen, with intermittent thawing performed using a 37°C water bath. The solution was then extruded through an Avanti Mini Extruder (Alabaster, Alabama) with a 0.1μm nuclepore polycarbonate membrane >11 times. Formed liposomes were then dialyzed against water in 3500Da MWCO dialysis cassettes for 24 hours.

Lipopeptisome Formulation

Formation of Lipopeptisomes (LP) was performed by combining the 5mM solution of 1:1 POPC:POPS liposomes in buffer with an equal volume of 2× concentrated solution of peptide in water, mixed and then incubated at 37°C for 30 minutes to allow for interpolation. The LP solution was then dialyzed against water for 24 hours using 300kD MWCO dialysis tubing, with frequent bath changes. Peptide loading was determined by measuring the absorbance of the purified particle solution at 220nm for peptide bonds using a Cary 60 UV-Vis spectrophotometer (Agilent Technologies, Santa Clara, CA), and concentration determined relative to a standard curve. Absorbance of blank liposomes was subtracted to normalize the signal. When necessary, the LP samples were concentrated in 0.5mL Eppendorf tubes on a

CentriVap Benchtop Vacuum Concentrator (Labconco, Kansas City, MO) for one hour, or until the desired volume had been achieved, for subsequent in vitro experiments.

Physiochemical and Mechanistic Characterization of Lipopeptisomes

Dynamic Light Scattering

Size characterization of LP particles was completed by dynamic light scattering (DLS) using a Zetasizer Nano ZS (Malvern Instruments Ltd, Worcestershire, UK). In a typical experiment a 60μL aliquot of the liposome solution in buffer was combined with an equal volume of peptide in water to achieve a final concentration of 0.01 – 1000 μM peptide. After incubating at 37°C for 30 minutes, the solutions were then diluted 1:10 in particle characterization buffer (150 mM BTP, 50 mM NaF, pH 7.4) and placed into a clean polystyrene cuvette. DLS was performed at 37°C with an equilibration time of 120 seconds, and average particle size determined from 6 replicates per sample. For LP stability studies, the particles were loaded with 100μM of each peptide, or left unloaded as a 'blank' control. Particles were diluted 1:4 in storage buffer (20mM Tris, 100mM NaCl, pH 7.4) and stored at 37°C, with DLS measurements performed at varied time points up to 110 days.

cryo-Transmission Electron Microscopy

Transmission electron cryomicroscopy was performed on blank liposomes and LP particles with each of the three anticancer peptides by adsorbing an aqueous aliquot of the sample onto a quantafoil grid. The grid was then vitrified via plunge freezing using a Vitrobot (FEI, ThermoScientific), and imaged at 300 kV using a Krios cryo-EM (FEI, ThermoScientific).

Confocal Microscopy

Giant Unilamellar Vesicles

In separate experiments, I utilized giant unilamellar vesicles (GUVs) as a model to visualize ACP integration into lipid membranes. Formation of GUVs was performed as previously described.[65] In brief, a solution of 1 wt% low-melting agarose was added to a 4-well chambered slide until it just covered the glass surface. The chambered coverglass was then dried on a 45°C hotplate for 1 hour until the agarose became translucent. After preparing a 3.75 mg/mL lipid solution of POPC, POPS, PE, and $PE_{rhodamine}$ in chloroform, 4μL was added to each chamber and a metal spatula gently dragged across the surface to evenly distribute the solution. The chambered coverglass was then lyophilized overnight to dry. Swelling of the GUVs occurred by adding 500μL of 150mM KCl solution to each well. After 15 minutes to allow for GUV fusion, 10μL of a 500μM fluorescein-labeled Lasioglossin solution was added to each chamber to initiate treatment. Slides were mounted onto an Olympus Fluoview 1000 confocal microscope and imaged using a PlanApo 60X/1.4 oil objective lens. 488nm and 543nm single photon lasers were used to visualize fluorescein and rhodamine fluorescence, respectively. Relative fluorescence (RF) was calculated using FIJI – ImageJ software by measuring the intensity of the fluorescein signal within a region of the GUV membrane and subtracting the background fluorescence from the surrounding bulk solution for each time point.

Dually Labeled LPs

Visualization of LP fusion with cancer cells, and subcellular localization of lipid and peptide particle components, was performed via confocal microscopy. For these experiments, Iprepared fluorescently labeled liposomes following the protocol above, with the exception that particles were composed of 49.5:50:0.5 POPC/POPS/PErhodamine. Loading of Lasioglossin into the particles was performed at a final peptide concentration of 100 μM, where fluorescein-labeled peptide was doped in at a

ratio of 10% with unlabeled Lasioglossin. A549 cells were seeded in 4-well coverglass chamber slides at 10,000 cells/well, and allowed to adhere overnight. Cells were treated with a final concentration of 20μM labeled LPs in media for 24 – 72 hours, or left untreated as controls. At each time point, the supernatant solution was removed, cells washed with cold PBS and fixed with 4% paraformaldehyde for 20 min. at room temperature. Cell nuclei were then stained by the addition of 2μg/mL Hoechst in PBS and incubated in the dark for 20 min. Slides were imaged on an Olympus Fluoview 1000 Confocal Microscope (Olympus, Shinjuku, Tokyo, Japan) with a PlanApo 60X/1.4 oil objective lens using 405nm, 488nm, and 543nm single photon lasers for DAPI, FITC, and rhodamine signals, respectively.

Structure and Kinetic Elucidation

Circular Dichroism

Circular Dichroism (CD) was performed on a J-1500 Circular Dichroism Spectrometer (JASCO, Oklahoma City, OK) to determine the secondary structure of the peptides upon integration into LPs. Here, 200μM of each peptide in 2× characterization buffer (15.1mM sodium phosphate dibasic heptahydrate, 0.49mM sodium phosphate monobasic monohydrate, and pH 7.4) was mixed with an equal volume of the liposomes (final lipid concentration of 2.5 mM). Wavelength spectra were measured from 180 to 260 nm at 37°C in a 1mm path length quartz cell. Mean residue molar ellipticity [θ], measured in ($deg*cm^2*dmol^{-1}$), was calculated from the following expression: $\theta_{meas}/(10*l*c*r)$ where θ_{meas} is measured ellipticity (mdeg), l is light path length (cm), c is molar concentration (mol/L), and r is number of amino acid residues.

OD_{600}

In parallel experiments to circular dichroism, the optical density, or absorbance at 600nm., was measured over time to determine rate of membrane disruption of model healthy and cancer mimicking liposomes. Measurements were taken every 30 seconds for the first 10 min. and every minute until 15 min. Values were normalized to respective liposomes in the absence of peptide.

Mechanistic Studies of MAD1

Confocal Microscopy

OVCAR-3 cells were seeded at 3 x 10^4 cells/well in a chambered coverslip and allowed to adhere for 24 hours. Cells were treated at the peptide IC_{50} as determined by preliminary experimentation in serum free media for 1 hour, 4 hours, and 10 hours. Serum free media was used as a negative control. After treatment incubation periods, cells were washed with cold PBS and fixed with 4% paraformaldehyde for 20 min. at room temperature. After washing with cold PBS, 2μg/mL Hoechst in PBS was added and left to incubate for 20 min. Slides were imaged on an Olympus Fluoview 1000 Confocal Microscope (Olympus, Shinjuku, Tokyo, Japan) with a PlanApo 60X/1.4 oil objective lens using 405nm and 488nm single photon lasers for DAPI and FITC, respectively.

Scanning Electron Microscopy

SEM was conducted using methods previously established.[66] In brief, A549 cells were first seeded onto uncoated glass coverslips in a 12 well plate at 30 x 10^3 cells/well, and allowed to adhere overnight. Next, the cells were treated with 10μM of peptide in serum free media for 1 or 4 hours, and a negative control also in serum free RPMI-1640. The cells were then washed with fresh serum free media, and then

fixed with cold 5% glutaraldehyde in 0.1mM sodium cacodylate and left overnight at 4ºC. The cells were subsequently rinsed three times with 0.1mM sodium cacodylate before an ascending ethanol dehydration series (25,50,70,85,90,95,100%) was performed. Each stage of the dehydration required 5 minutes in solution before proceeding in the series. The cells were then stored in 100% ethanol before transferring to a Leica EM CPD300 Critical Point Dryer (Buffalo Grove, Illinois). Dried samples were then mounted onto metal SEM stubs using double sided carbon tape, and sputter coated with Au/Pd 60:40 using a Bal-tec SCD-050 Sputter Coater (Capovani Brothers Inc., Scotia, New York). Finally, samples were imaged using a Zeiss SIGMA VP-FESEM (Thornwood, New York) using secondary electron imaging. Experiments were performed in duplicate.

Flow Cytometry

FITC-Annexin V/PI

OVCAR-3 cells were first seeded at 2 x 10^5 cells/well in 12 well plates. The cells were then allowed to adhere overnight. Treatments were conducted at $1\times IC_{50}$ of MAD1 at 2 and 24 hours in culture media adjusted to 5% serum. Wells were left in 5% serum media for negative and compensation controls. Cells were then trypsinized, washed in cold PBS, and centrifuged at 3,000 rpm at 15°C for 5 min. After the supernatant was aspirated, the cells were resuspended in 100µL of Annexin V Binding Buffer. In the dark, 5µL of FITC Annexin V and 10µL of Propidium Iodine solution were added to the cells, with compensation controls of a negative control with no staining, a FITC Annexin V only control, and a PI only control. The cells were then vortexed gently to combine and allowed to incubate for 15 min. at room temperature. 400µL of Annexin V Binding Buffer was then added to each tube and stored on ice prior to analyzing by flow cytometry.

Flow cytometry was conducted on a LSRFortessa Flow Cytometer (BD Biosciences, Franklin Lakes, New Jersey) using 488nm and 532nm lasers for FITC and PE-Texas Red signals to detect Annexin V and PI, respectively. Compensation was completed for 10,000 cells, and experiments were conducted over 20,000 cells.

Tetramethylrhodamine, ethyl ester (TMRE) flow cytometry

OVCAR-3 cells were treated with the indicated concentrations of MAD1 peptide for 48 hours or the positive control FCCP (2-[2-[4-(trifluoromethoxy)phenyl]hydrazinylidene]-propanedinitrile) for 5 min. (5μM). Cells were incubated for 30 min. with 200nM TMRE, washed twice with PBS, and analyzed for fluorescence by flow cytometry on a BD FACSCanto 10 (BD Biosciences, Franklin Lakes, New Jersey).

Western Blot for Apoptotic Factors

For western blots, OVCAR-3 cells were first seeded at 2.5 x 10^5 cells/well in a 6 well plate and allowed to adhere overnight. Cells were then treated in 5% FBS media with $1\times IC_{50}$ and $2\times IC_{50}$, with untreated controls of media alone. Following 2 or 48 hours of treatment, the whole-cell protein lysates were prepared in RIPA buffer (50mM Tris·NaOH at pH 7.4, 150mM NaCl, 1% IGEPAL-CA630 [octylphenoxy poly(ethyleneoxy)ethanol], 0.5% sodium deoxycholate, 0.1% SDS, 2mM EDTA, protease/phosphatase inhibitors) by first scraping the bottom of the well and subsequently briefly sonicated. The lysates were centrifuged to clear cellular debris, separated by 12% SDS-PAGE, and transferred to a 0.2μm Nitrocellulose Membrane using the Bio-Rad Trans-Blot Turbo transfer machine (Bio-Rad, Hercules, CA, USA) according to the manufacturer's protocols. The blot was incubated in 5% Immunoanalytical Grade Non-fat Dry Milk for 1 hour, followed by incubation with antibodies against cleaved caspase-3 (1:1000) or actin (1:1000) at 4°C for 16 hours. The blots were then incubated with 1:2000 dilution in 1X BSA of anti-mouse or anti-

rabbit antibodies for 1 hour before washing with TBST three times for 15 min. and developing using Pierce ECL system according to the manufacturer's protocol.

Mammalian Cell Studies

Cell Culture Conditions

All cells were cultured using standard culture conditions at 37ºC, 5% CO_2, and 95% humidity. A549 (CCL-185), HeLa (CCL-2), OVCAR-3 (HTB-161), MDA-MB-231 (HTB-26), T24 (HTB-4), and NCI/ADR-RES were cultured in RPMI-1640 supplemented with 10% v/v fetal bovine serum (FBS), 2mM L-Glutamine (L-Gln), and 0.05 mg/mL gentamycin. Caco-2 (HTB-37) cells were cultured in DMEM supplemented with 10% v/v (FBS), 2mM L-Gln, and 0.05 mg/mL gentamycin. HUVEC (PCS-100-010) cells were cultured in Vascular Cell Basal Media (PCS-100-030) supplemented with an Endothelial Cell Growth Kit-VEGF (PCS-100-041) and 10µg/mL gentamycin in culture flasks coated with 0.1% gelatin by incubating at 37°C for 15 minutes. NL-20 (CRL-2503) cells were cultured in Ham's F12 supplemented with 1.5 g/L sodium bicarbonate, 2.7 g/L glucose, 2.0 mM L-glutamine, 0.1 mM nonessential amino acids, 0.005 mg/ml insulin, 10 ng/ml epidermal growth factor, 0.001 mg/ml transferrin, 500 ng/ml hydrocortisone and 4% fetal bovine serum, as advised by American Type Culture Collection (ATCC).

Cell Viability Assay

MTT assay was conducted after cell treatment period by first aspirating treatment solutions before the addition of 100µL of 0.5mg/mL thiazolyl blue tetrazolium bromide in media to each well and incubating for 2-3 hours. Cells were subsequently lysed and the formazan byproduct solubilized by addition of 100µL DMSO. After incubating for an additional 10 min., absorbance was read at 540nm on with a microplate

reader (Biotek, Winooski, VT). Percent viability was calculated with the following equation: $(Absorbance_{treatment} - Absorbance_{negative\ control})/(Absorbance_{positive\ control} - Absorbance_{negative\ control})$ X 100%.

Lipopeptisome Treatments

For cell viability experiments with lipopeptisomes, cells were seeded into a 96 well plate at 2 x 10^3 cells/well for A549 and HeLa, and 5 x 10^3 cells/well for HUVEC. Cells were allowed to adhere overnight before the media was aspirated and treatments of free peptides or LP formulations added in 10 fold dilutions to achieve a final concentration of 0.001μM - 100μM. Blank media and 20% DMSO were included as negative and positive controls, respectively. Treatments were incubated for 72 hours before measurement of cell viability via MTT assay. Experiments were performed in duplicate with 6 internal replicates.

Individual Anticancer Peptide and Chemotherapeutic Treatments

For cytotoxicity experiments, cells were first seeded in 96 well plates at 5 x 10^3 cells/well for A549, OVCAR-3, T24, and NCI/ADR-RES cells, and 10 x 10^3 cells/well for HUVEC and NL20 cells. After 24 hours of incubation to allow the cells to adhere, the media was aspirated and 100μL of treatments prepared in media with 5% FBS were added to each well; blank media and 20% DMSO served as negative and positive controls, respectively. Treatments were allowed to incubate for 48 hours, followed by cell viability determination by MTT assay. In brief, wells were aspirated and replaced with 100μL of 0.5 mg/mL thiazolyl blue tetrazolium bromide dissolved in media. The plates were allowed to incubate for 2-3 hours and were then lysed with 100μL of DMSO to dissolve the converted formazan product. Absorbance of the wells was measured via a microplate reader (Biotek, Winooski, VT) at 540nm; percent viability was calculated by subtracting the positive control and normalizing to the negative control.

For individual peptide cytotoxicity experiments, MAD1, DAP1, and DAP2 treatments were serially diluted to 100 – 0.001μM concentrations. For individual chemotherapeutic experiments, doxorubicin, paclitaxel, and cisplatin were diluted 1:10 six times from 100μM, 100nM, and 100μM, respectively. All treatments were prepared first as a stock solution in water and subsequently diluted into standard media with 5% FBS; paclitaxel and cisplatin stock solutions were first prepared in DMSO before diluting into media with a final DMSO concentration <0.1%. All experiments were performed with n>6.

Combinatorial Peptide + Chemotherapeutic Treatments

For combinatorial cytotoxicity experiments, 96 well plates were set up in a checkerboard fashion such that peptide decreased in 1:10 concentration dilutions in one direction and chemotherapeutic decreased in 1:10 concentration dilutions in the orthogonal direction. 2× treatments were combined prior to cell administration for a final 1× concentration to prevent individual treatment effects. Experiments were performed in triplicate and heat maps were generated with MATLAB using logarithmic interpolation to obtain drug IC_{50} values at 20μM MAD1.

Spheroid Culturing

OVCAR-3 cells were cultured using RPMI 1640 supplemented with 5% FBS and 1% penicillin-streptomycin. EOC patient-derived cells were cultured in 1:1 MCDB-105: M199 supplemented with 10% FBS and 10% penicillin-streptomycin. EOC patient-derived cells were provided by Dr. Katherine M. Aird under an Institutional Review Board-approved protocol. EOC patient-derived cells were collected from patient ascites fluid after paracentesis procedures. Cells were routinely tested for mycoplasma as previously described.[67] OVCAR-3 and patient-derived cells (EOC15, EOC17, and EOC19) were seeded at 1 x 10^5 cells/well in ultra-low attachment (ULA) plates. 24 hours after seeding, spheroids were treated alone or in

combination with 2μM cisplatin and/or 4μM MAD1 peptide for 48 hours. After 48 hours, 10X images were taken of the spheroids (Nikon Elements Ts2, Nis Elements F 4.51.00). Spheroid length and width was calculated using ImageJ. Spheroid volume was calculated using the following equation $\frac{(W^2)*L}{2}$. Experiments were performed in triplicate at least two independent times.

Bacterial Studies

Bacterial Growth Conditions

For bacterial assays, bacteria were cultured according to the following established methods.[68] *Bacillus subtilis (168)* was cultured in lysogeny broth (LB). *Escherichia coli, Pseudomonas aeruginosa* (PAO-1), Methicillin-resistant *Staphylococcus aureus* (MRSA; NRS72), *and* Methicillin-sensitive *Staphylococcus aureus* (MSSA; NRS72) were cultured in cation adjusted Mueller-Hinton broth (CAMHB). *Mycobacterium tuberculosis* (H37Ra) was cultured in Middlebrook 7H9 supplemented with 0.05% (v/v) polysorbate 80, 0.5% (v/v) glycerol and 10% (v/v) oleic acid-albumin-dextrose-catalase (OADC). Each culture was grown in a shaking incubator at 37ºC at 200 rpm, according to guidelines provided by the Clinical and Laboratory Standards Institute (CLSI).

Bacterial Minimum Inhibitory Concentration Assay

For MIC studies, peptide was first prepared in water at 320μL (4X) and diluted 1:2 in appropriate treatment broth. Bacteria were prepared in appropriate media and diluted to an Optical Density at 600nm (OD_{600}) of 0.002. Next, 50μL of treatment broth was added to each well in rows 2-8 of a 96 well plate, with the first three columns containing untreated broth as a negative control. In row 1, 100μL of the 2× peptide in broth was added. Using a multi-channel pipette, 50μL of the 2× peptide solution was diluted 1:2 in the

subsequent row and repeated for all rows. 50µL of bacteria was added to each well, incubated for 24 hours, and read using visual evaluation. The MIC, or minimum inhibitory concentration, was determined by the lowest concentration with a significant reduction in bacteria pellet presence compared to the negative control.

Hemolysis

Hemolysis studies began by obtaining fresh human blood samples and isolating red blood cells via centrifugation at 3,460 rpm for 10 min. at 4°C. The plasma and buffy coat layers were removed and hRBCs washed three times in un-supplemented RPMI. A 0.25% v/v solution of the washed hRBCs was prepared in RPMI, and a 75 µL aliquot added per well to a 96 well plate. Equal volume of free peptide or LP solutions were added to the RBC sample and gently mixed via pipette to achieve a final equivalent peptide concentration of 10 - 100 µM. Blank RPMI or 1% Triton-X100 were used as negative and positive controls, respectively. Plates were then incubated at 37°C for 24 hours, before centrifugation at 4,000 rpm for 10 min. at 4°C to pellet intact hRBCs. 100 µL of the hRBC supernatant was added to a clean 96 well plate and absorbance of released hemoglobin measured at 415 nm in a microplate reader (Biotek, Winooski, VT). The following equation was used to calculate percent hemolysis: $(Absorbance_{treated}-Absorbance_{negative\ control})/(Absorbance_{positive\ control}-Absorbance_{negative\ control})$ X 100%.

Statistical Methods

Re-engineering Antimicrobial Peptides into Oncolytics Targeting Drug-Resistant Ovarian Cancers

Cell viability experiments were completed n>6 in two independent experiments and analyzed using GraphPad Prism 8 to fit curves and calculate IC_{50} values using inhibitor vs. normalized response non-

linear regression model. IC_{50} values are reported as mean values ± standard deviation. For bacterial MIC experiments, values are reported as the average of 3 replicates. Pore size frequency distribution was completed by ImageJ FIJI on 5 independent cells and n>125 pores from SEM images. UV-Vis OD_{600} and CD spectra are means of 5 and 3 replicates, respectively and reported as mean ± standard deviation. Individual UV-Vis and CD spectra, as well as fluorescent confocal and TEM micrographs, shown are representative plots from three individual experiments. CD data is with a variance in ellipticity of 0.2 millidegrees at each wavelength. Relative fluorescence data calculated from fluorescent confocal images represents the average of 10 independent measurements ± standard deviation. For spheroid volume analysis, a Kruskal-Wallis test and Dunn's multiple comparisons test was performed using GraphPad Prism 8.

Lipopeptisomes: Anticancer Peptide-Assembled Particles for Fusolytic Oncotherapy

Dynamic light scattering and absorbance data is the average of three replicates ± standard deviation. Each UV-Vis and CD spectra, as well as fluorescent confocal and TEM micrographs, shown are representative of three individual experiments. CD data is with a variance in ellipticity of 0.2 millidegrees at each wavelength. Relative fluorescence data calculated from fluorescent confocal images represents the average of 10 independent measurements ± standard deviation. Cytotoxicity data is represented as an average of three independent experiments ± standard deviation. GraphPad Prism 5 software was used to fit cytotoxicity curves and calculate IC50 values employing a log(inhibitor) vs. normalized response non-linear regression model. For hemolysis experiments each treatment condition was performed in triplicate and average % hemolysis ± standard deviation calculated.

Chapter 3
Results and Discussion

Re-engineering Antimicrobial Peptides into Oncolytics Targeting Drug-Resistant Ovarian Cancers

Design and activity of de novo ACPs

To begin our design of new ACPs, we turned to the model antimicrobial peptide MAD1 (myco-membrane associated disruption 1 sequence). This sequence, recently characterized by our lab,[69] preferentially disrupts mycobacterial membranes to elicit tuberculosis-specific killing. Key to MAD1's bactericidal action is its ability to adopt a facially amphiphilic alpha helix that is defined by a hydrophobic, tryptophan-rich surface (**Fig. 4a**). Intermolecular zippering of tryptophan side chains enables supramolecular assembly of MAD1 peptides to form a lytic nanostructure within the tuberculosis pathogen cell wall. Given its antimicrobial importance, we first investigated the role of this tryptophan-rich helical surface on the potential anticancer activity of MAD1. To do this we designed two ACP analogues, DAP1 and DAP2 (*de novo* designed anticancer peptide), in which both sequences exhibit variations in hydrophobic amino acid packing and spatial display relative to the MAD1 template. For DAP1, the cationic and hydrophobic faces of the helix are spatially segregated with respect to each other (see helical wheel in **Fig. 4b**, bottom), resulting in a more uniform angular alignment of tryptophan residues in the axial direction. In order to accommodate this dense packing of hydrophobic groups, the number and spacing of lysine and arginine residues was altered for the DAP1 scaffold. Collectively this design led to an increase in sequence hydrophobicity (defined by logD value[45]) and a decrease in helical hydrophobic moment (a vector-based measure of helix amphiphilicity[70]) of DAP1 compared to MAD1 (**Table 1**). Conversely, DAP2 is designed such that tryptophan residues are axially isolated to only the N-terminal half of the peptide, leading to a decrease in the overall hydrophobic surface area relative to MAD1 (**Fig. 4c**). This results in a significant decrease in hydrophobicity, as defined by a reduction of its logD value, and corollary

increase in hydrophobic moment for DAP2 relative to MAD1. Together, these peptide analogues allow us to systematically evaluate how changes in sequence logD and hydrophobic moment influence their cytotoxic effects; with the expectation that anticancer potency will follow DAP1 > MAD1 > DAP2.

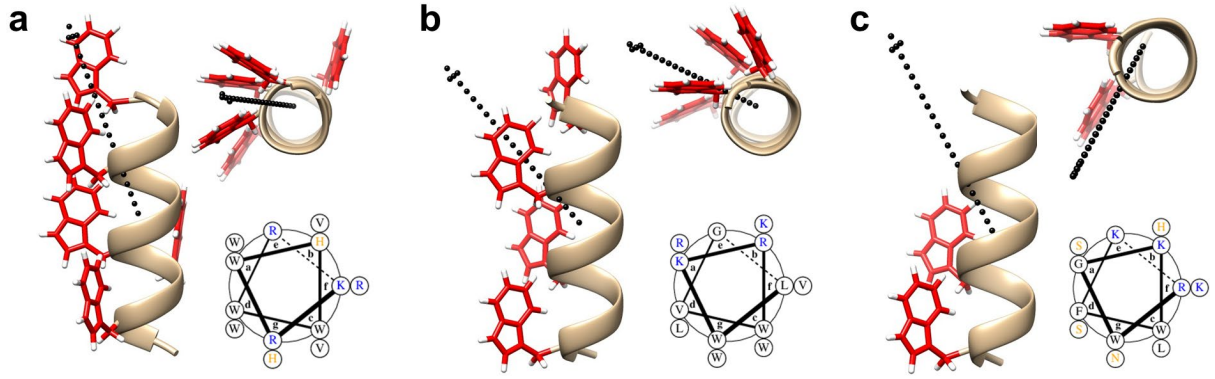

Figure 4. Rational design of de novo anticancer peptides. Minimized model of (**a**) MAD1, (**b**) DAP1, and (**c**) DAP2 peptide helices. For all panels, Left: helical profile; Top right: axial view (red = tryptophan residues). Vector of the hydrophobic moment shown as dotted black arrow. Bottom right: helical wheel (black = hydrophobic, blue = basic, orange = polar residues).

Table 1. Sequence and physiochemical properties of *de novo* designed ACPs

Peptide	Sequence[a]	Sequence Length	Formal Charge[b]	logD	Hydrophobic Moment
MAD1	KRWHWWRRHWVVW-NH_2	13	+7	-3.41	14.828
DAP1	LWKRWVGVWRKWL-NH_2	13	+5	-3.23	13.879
DAP2	RWGKWFKKNSHLS-NH_2	13	+5	-9.37	15.250

[a] All peptides are prepared with amidated C-terminus

[b] Formal charge includes N-terminal amine. Histidine considered partially protonated for purposes of formal charge calculation.

To test this assertion, we measured the cytotoxicity of each sequence against a panel of human cancer cell lines, as well as non-cancerous controls (**Fig. 5a**, **Table 2** and **Suppl. Fig. 5**). As predicted, DAP1 was the most potent ACP of the three sequences, with IC50 values that ranged from 8.6 – 15.3μM, dependent on cell line. MAD1 displayed preferential activity towards the ovarian carcinoma cell line OVCAR-3 (IC_{50} = 14.2μM, Fig. 5a), moderate activity against A549 (lung carcinoma) and NCI/ADR-RES (drug resistant ovarian cancer) cells, and was inactive towards T24 (bladder cancer). Consistent with our expectations, DAP2 was inactive towards all four of the tumor cell lines tested.

Interestingly, although DAP1 was the most potent ACP of the three peptides, it showed nearly equal toxicity against the two non-cancerous cell lines tested: human umbilical vein endothelial cells

(HUVEC) and human lung epithelium (NL20). Accordingly, this defines therapeutic indices, a quantitative measure of relative drug safety, for DAP1 of ≤ 2.3 (Table 2). MAD1 on the other hand was well tolerated by both control cell lines and, as result, generally possessed superior therapeutic indices compared to DAP1. Notably, MAD1 displayed an index of 7 towards OVCAR-3 cells, suggesting a distinct selectivity of the peptide towards ovarian cancers; an assertion we later confirm in *ex vivo* studies.

Thus far, our cytotoxicity data supports the claim that AMPs can be re-designed to afford new ACP candidates. Given the shared mechanisms of action between these two classes of peptides, the reverse should also be true: ACPs can function as AMPs. To test this assertion, we measured the antimicrobial activity of all three ACPs against a polymicrobial panel (**Table 3**). In line with our hypothesis, MAD1 and DAP1 both displayed bactericidal activity, with DAP1 generally showing more potent broad-spectrum effects relative to the MAD1 peptide. Conversely, DAP2 is inactive towards all six of the bacterial lines tested.

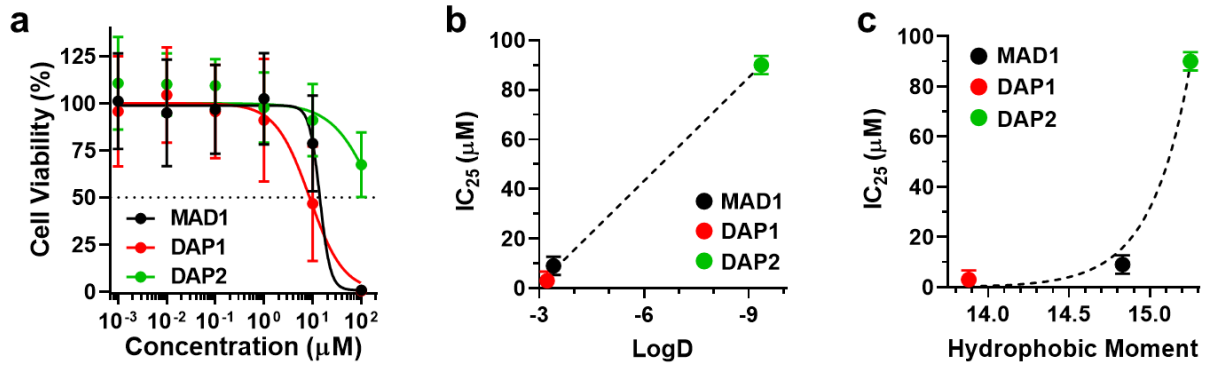

Figure 5. ACP cytotoxicity and structure-activity relationships. (**a**) Cytotoxicity curves for MAD1, DAP1 and DAP2 peptides against OVCAR-3 ovarian carcinoma cells. Curves for all four cancer cell lines tested are shown in Suppl. Fig. 5. Dashed line indicates IC_{50}. Relative change in OVCAR-3 IC_{25} value as a function of (**b**) sequence hydrophobicity (logD) and (**c**) helix facial amphiphilicity (hydrophobic moment). Data is fit using GraphPad Prism software, and dashed lines of model fit included to guide the eye.

Table 2. Peptide cytotoxicity towards cancerous and non-cancerous cell lines

	Cancerous (IC_{50}, μM)				Healthy (IC_{50}, μM)		Therapeutic Index[a]			
Peptide	**A549**	**OVCAR-3**	**NCI/ADR-RES**	**T24**	**HUVEC**	**NL20**	**A549**	**OVCAR-3**	**NCI/ADR-RES**	**T24**
MAD1	36.2	14.2	85.6	>100	>100	76.9	2.8	7.0	1.2	-
DAP1	11.9	8.6	14.0	15.3	19.5	19.0	1.6	2.3	1.4	1.3
DAP2	>100	>100	>100	>100	>100	>100	-	-	-	-

[a] Therapeutic index of each peptide for indicated cell type relative to HUVEC controls ($IC_{50\text{-HUVEC}}/IC_{50\text{-indicated cell}}$)

ACP structure-activity relationships and ovarian cancer specificity

To better understand the physiochemical drivers of ACP toxicity in tumor cells we further examined how anticancer potency of these peptides is influenced by their hydrophobicity (logD, **Fig. 5b**) and facial amphiphilicity (hydrophobic moment, **Fig. 5c**). For these analyses we utilized cytotoxicity data from the OVCAR-3 cell line and plotted the appropriate IC_{25} value of each sequence (IC_{25} was chosen as DAP2 did not achieve an IC_{50} at the concentrations tested; see green data in Fig. 5a). Results in Fig. 5b demonstrate a linear relationship between peptide toxicity and logD value for the sequences tested. Conversely, we observed an exponential dependence of ACP activity and hydrophobic moment of each peptide (Fig. 5c). Taken together, this suggests that the membranolytic potential of a given ACP is largely dependent on its lipophilicity. Interestingly, our data also indicates there may exist an amphiphilicity threshold that differentiates active from inactive sequences. In particular, data in Fig. 5c suggests that peptide helices with a hydrophobic moment <15 are sufficiently amphiphilic to interpolate into the lipid bilayer of tumor cells and form lytic assemblies. This further validates the claim of shared molecular mechanisms of action between ACPs and AMPs, as it is well established that hydrophobicity and amphiphilicity are important factors in the activity of antimicrobial peptides.[30,71]

Table 3. Minimum inhibitory concentration (MIC) of *de novo* ACPs

		MIC (μM)		
	Bacteria	**MAD1**	**DAP1**	**DAP2**
Gram Positive	*B. subtilis (168)*	**0.2**	**<0.6**	**>80**
	MS S. aureus	**>80**[a]	**7**	**>80**
	MR S. aureus	**>80**[a]	**5**	**>80**
Gram Negative	*P. aeruginosa*	**50**[a]	**20**	**>80**
	E. coli	**25**	**10**	**>80**
Mycobacteria	*M. tuberculosis*	**2.5**[a]	**20**	**>80**

[a] Data reported in reference [69]

Our cell-based studies collectively demonstrate that MAD1 preferentially targets and disrupts cancer cell membranes over that of normal, healthy counterparts. To mechanistically investigate this, circular dichroism (CD) spectroscopy was performed to monitor changes in peptide secondary structure in the absence and presence of normal or cancerous liposomal membrane analogues. CD spectra shown in **Fig. 6a** demonstrate that MAD1 adopts an α-helical conformation in aqueous solutions, with characteristic minima in ellipticity at 204nm and 216nm. An exciton band at 228nm is indicative of interactions between aromatic indole chromophores as a result of intermolecular tryptophan pairing between peptides.[72] When mixed with liposomes mimicking the composition of normal mammalian cell membranes (72:23:5 POPC:DOPE:POPS),[73] MAD1 largely maintains its α-helical structure. A slight red-shift (+2 nm) in both the Trp-Trp ellipticity maximum (230nm) and α-helical minima (206nm and 218nm) suggests MAD1 benignly adsorbs to the surface of normal membranes.[74] However, when mixed with cancer membranes a dramatic absorption flatting of MAD1's CD signal is observed (Fig. 6a, black data). These changes can be attributed to the organization of peptide chromophores during their ordered interpolation within regions of high lipid density.[74] This indicates that MAD1 is able to rapidly assemble within the cancer cell

liposomal membrane to cause lysis, which is further corroborated by an increase in solution optical density (**Fig. 6b**) and the generation of macroscopic lipid fragments (Fig. 6b inset and **Suppl. Fig. 6**). Conversely, MAD1 did not lyse the healthy liposomal counterparts.

DAP1, on the other hand, evolves from an ensemble of random coil conformations in aqueous solution to a CD spectrum indicative of sheet-rich and tryptophan stacked conformations in the presence of both normal and cancer cell membranes, as indicated by ellipticity minima at 212 and 230nm, respectively (**Fig. 6c**).[75] Parallel optical density measurements demonstrate that, although DAP1 rapidly integrates into cancer cell liposomes, it does not completely lyse the membranes and instead re-organizes into stable peptide-lipid complexes (**Fig. 6d** and Suppl. Fig. 6). Collectively, our biophysical data suggests that MAD1 preferentially engages tumor cells to elicit selective membranolytic activity, while DAP1 is unable to discriminate healthy from cancerous membranes; providing further mechanistic insight into the differential cell cytotoxicity profiles of the two peptides (Table 2).

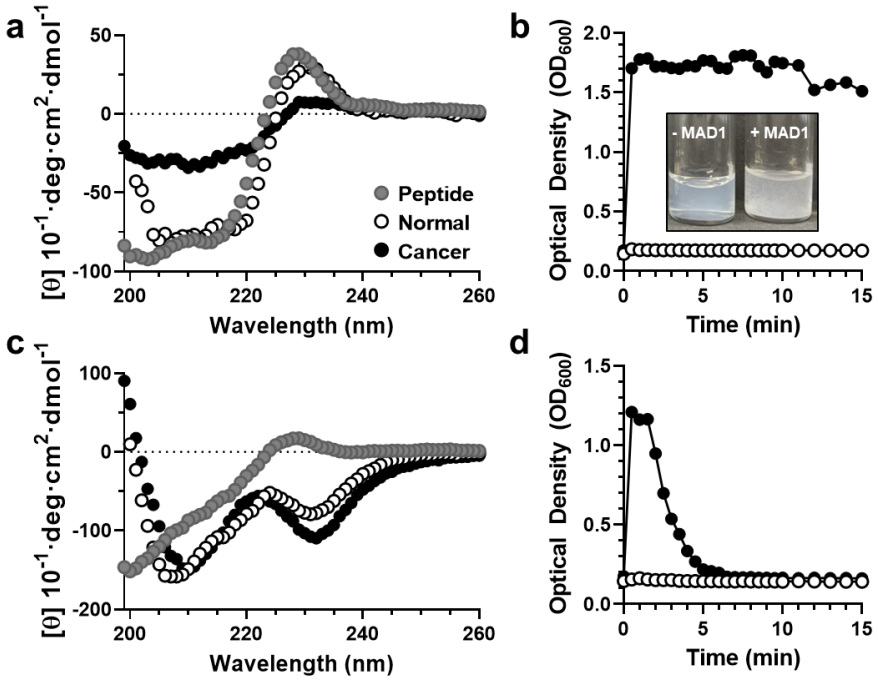

Figure 6. Tumor membrane-templated ACP assembly. (**a**) Circular dichroism spectra of the MAD1 peptide in aqueous solution (●), or in the presence of normal (○) and cancer cell (●) membrane models. (**b**) Relative disruption of normal (○) and cancer (●) model membranes by the MAD1 peptide, as determined from optical density measurements (OD_{600}). *Inset*: image of cancer membrane liposomal solution before (-MAD1) and after (+MAD1) treatment with the peptide. Formation of large flocculates provides visual confirmation of liposome disruption. (**c**) Circular dichroism spectra and (**d**) optical density measurements of DAP1 in the absence or presence of model membranes (● = no membrane, ○ = normal membrane, ● = cancer membrane).

MAD1 mechanism of action

Recent studies suggest that many ACPs exploit diverse physical (lytic) and biochemical (apoptotic) modes of toxicity, which operate in either an independent or coincident fashion depending on the cell type.[32,76,77] This is exemplified by our current study, in which DAP1 displayed similar potency across all cell lines tested, whereas MAD1 demonstrated a strong preference for OVCAR-3 ovarian carcinoma cells (Table 2). Thus, DAP1 may employ a cell-type agnostic mechanism, while MAD1 potentially elicits a combination of necrosis and apoptosis that is particularly potent towards ovarian carcinomas. To investigate this, we monitored the time-dependent subcellular localization of a fluorescently-labeled MAD1 analogue in OVCAR-3 cells (**Fig. 7a**). These microscopy studies show that, shortly after addition, MAD1 localizes to the membranes of treated ovarian cancer cells. Interestingly, exposure of OVCAR-3 to MAD1 evoked a ruffled morphology of the cellular surface, particularly at the migratory leading edges (**Fig. 7b**). This is complemented by the appearance of micron-sized defects in the plasma membrane. After this initial surface binding, MAD1 translocates to the cytoplasm (**Fig. 7c**) and subsequently localizes to the nuclear envelope (**Fig. 7d**). To confirm these observations, as well as directly visualize MAD1-induced damage to the plasma and nuclear membranes, we performed scanning electron microscopy. SEM imaging confirms that MAD1 rapidly assembles within the membranes of cancer cells to form micron-sized pores (**Fig. 7e**, untreated control image shown in **Suppl. Fig. 7**). These peptide-induced perturbations appear preferentially within cell pseudopodia (see white arrows in Fig. 7e) and possess an average diameter of 0.8μm (**Fig. 7f**). Acute changes in lipid geometry at these extending pseudopods, which experience a local negative membrane curvature,[78] suggests that the amphipathic MAD1 peptide subsequently exploits these flexures for

preferential bilayer interpolation.[79,80] Importantly, these membrane destabilizing effects are accompanied by peptide-mediated degradation of the cell's nuclear envelope (**Fig. 7g**), which also experiences a high degree of membrane curvature.[81] Although ACP-mediated damage to plasma and mitochondrial membranes has been observed previously, to our knowledge MAD1 is the first example of an amphipathic peptide with the capacity to preferentially bind and disrupt the nuclear envelope.

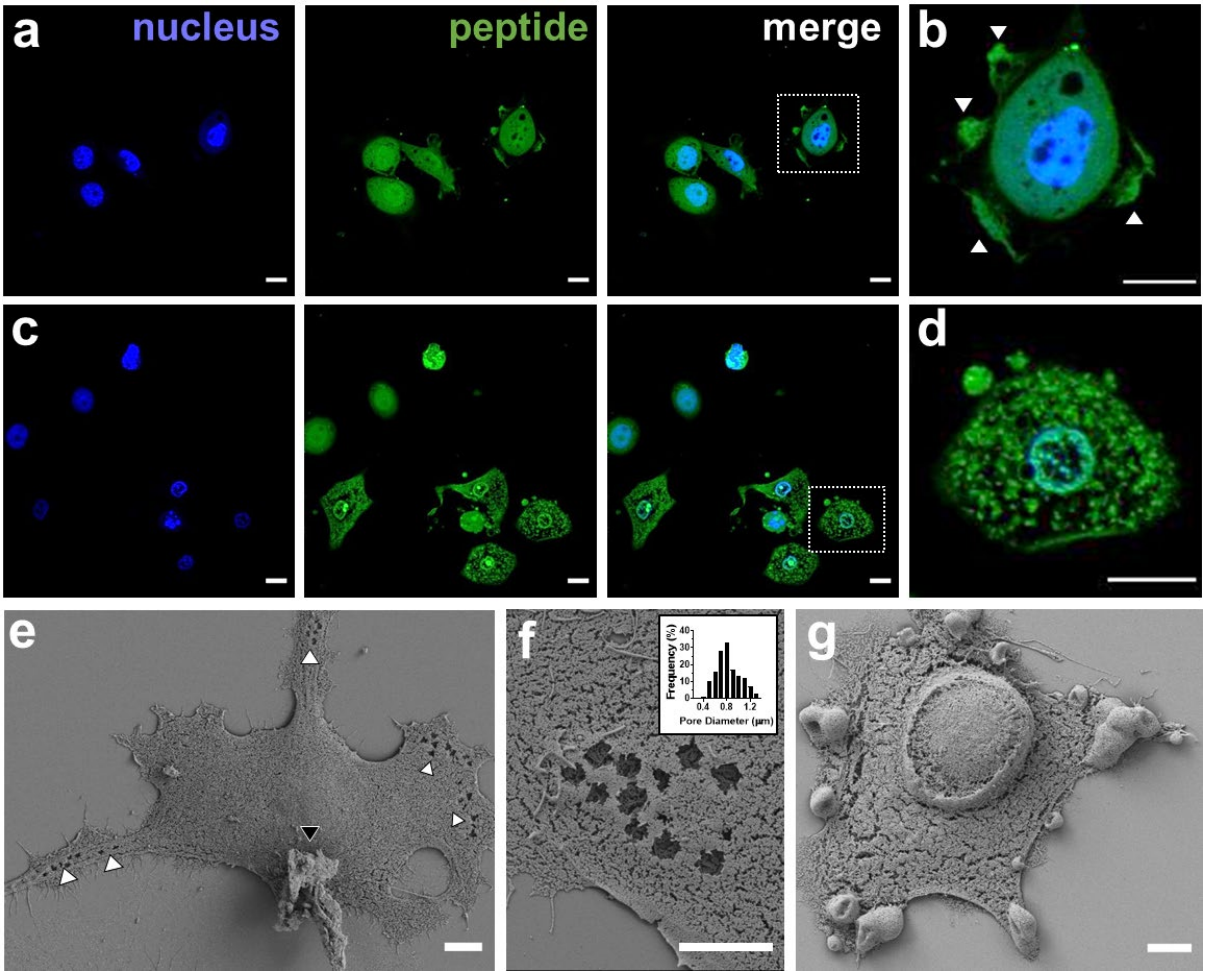

Figure 7. MAD1 integration into cancer cells and subcellular trafficking. (**a**) Confocal micrographs of OVCAR-3 ovarian carcinoma cells treated with 14μM of fluorescein-labeled MAD1 for 1 hour. (**b**) Magnification of boxed cell in merged image of panel a. Membrane ruffling marked by white arrows. (**c**) Micrographs of OVCAR-3 cells following a 10 hour incubation with MAD1. (**d**) Magnification of boxed cell in merged image of panel c demonstrating peptide localization to the nuclear envelope. Scale bars for panels a-d = 15μm. (**e**) SEM image of membrane-templated MAD1 pores in MAD1-treated A549 cells; surface pores (white arrows) and leakage of intracellular contents (black arrow) highlighted. (**f**) Magnification of peptide-induced pores. *Inset:* Histogram of pore diameter. (**g**) SEM micrograph of nuclear membrane damage by the MAD1 peptide. Scale bar for panels e-g = 5μm.

Taken together, this suggests that insertion and supramolecular assembly of MAD1 within the membranes of cancer cells alters bilayer tension and destabilizes the protective nuclear enclosure. Accordingly, this may lead to the induction of apoptotic signaling cascades after initial necrotic priming of cancer cells by the peptide. To test this, we performed annexin V-PI flow cytometry assays following treatment of OVCAR-3 cells at the IC_{50} of MAD1 for 2 and 24 hours (**Fig. 8a**). Results show that, although MAD1 causes considerable cell necrosis (16% of population) at early time points (2 hours), the majority of cells (65%) adopt a late apoptotic phenotype (**Fig. 8b**). After 24 hours cells predominantly occupy early

(19%) and late (77%) apoptotic stages. This rapid induction of apoptosis may be caused by mitochondrial depolarization, which can activate caspase cascades within 30 min. To investigate this, we utilized a TMRE-staining flow cytometry assay to evaluate mitochondrial transmembrane potential in OVCAR-3 cells after a 48 hour incubation with the peptide. Here, intact mitochondria take up the TMRE dye and brightly fluoresce, while depolarized or inactive mitochondria fail to sequester the TMRE fluorophore. Results in **Fig. 8c** and **Suppl. Fig. 8** show that OVCAR-3 mitochondrial integrity is generally unchanged in the presence of MAD1, and at certain peptide concentrations appears to increase. This indicates that MAD1 does not affect mitochondrial activity to potentiate intrinsic apoptotic signaling in treated cancer cells. Yet, parallel western blot experiments confirm the presence of cleaved caspase 3, a common effector of both intrinsic and extrinsic apoptotic pathways, in MAD1-treated OVCAR-3 cells (**Fig. 8d**). Taken together, this indicates that MAD1's early lytic effects are complemented later by the induction of extrinsic apoptotic pathways. Given that the peptide assembles at the surfaces of cancer cells (**Fig. 8e-g**), the most likely explanation for this is that membrane-templated supramolecular assembly of MAD1 leads to ligation of extrinsic FAS, TNF or TRAIL death receptors.[82]

However, our western blot data, which demonstrates that MAD1-mediated activation of caspase 3 does not occur until 48 hours, contradicts the annexin V-PI assays which show that the peptide induces apoptosis within 2 hours (Fig. 8a and b). One explanation for these incongruous results in that early MAD1-mediated poration of the cancer cell plasma membrane allows the cytosolic diffusion of the otherwise cell-impermeant annexin-V probe, which can then bind its phosphatidylserine lipid target on the inner leaflet. An alternative hypothesis is that membrane interpolation of MAD1 rearranges lipids in the asymmetric bilayer and physically translocates phosphatidylserine to the outer leaflet, where it then binds the annexin-V protein. In both scenarios MAD1 treated cells would stain positive for apoptosis at these early time points, but ultimately experience an oncolytic mechanism. Similar results have been observed for other AMPs tested for antitumor activity, which rapidly induce late apoptotic and necrotic phenotypes in treated cancer cells.[83–86]

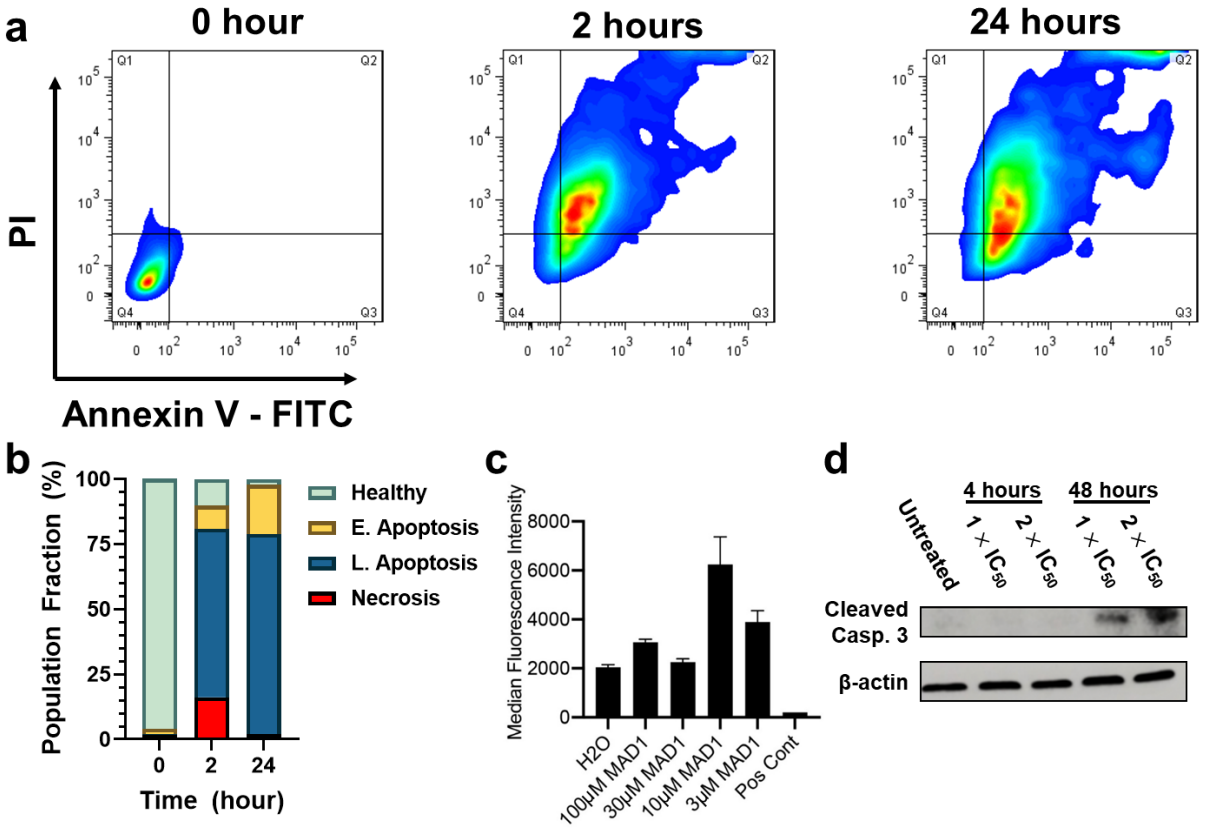

Figure 8. Mechanism of antitumor action by MAD1. (**a**) Representative plots from flow cytometric PI/Annexin V-FITC apoptosis assays of OVCAR-3 cells treated with 14μM of MAD1 for 2 or 24 hours. (**b**) Quadrant quantification of flow cytometry data defining the healthy cell population from necrotic cells, or those in early and late apoptosis, as a function of incubation time with the peptide. (**c**) Quantification of TMRE fluorescence for OVCAR-3 cells treated with varying concentrations of MAD1. Water or FCCP were included as a negative and positive control, respectively. (**d**) Western blot analysis of cleaved caspase 3 from OVCAR-3 cells after incubation with medium alone (untreated), or MAD1 at 1× and 2× its IC_{50} for 4 and 48 hours.

Anticancer synergy

Given MAD1's selective action against ovarian cancer cells, and its co-induction of physical (lysis) and biochemical (extrinsic apoptosis) death pathways, we next tested its potential to synergistically enhance the potency of three chemotherapeutics commonly used to treat ovarian carcinomas: Doxorubicin (Dox), Paclitaxel (Ptx) and Cisplatin (Cis). Remarkably, in both drug-refractory (OVCAR-3) and multidrug resistant (NCI/ADR-RES) ovarian cancer lines MAD1 potently synergizes with all three therapeutics tested (**Fig. 9a**, **Suppl. Table 1** and **Suppl. Fig. 9**). As a notable example, co-treatment of multidrug resistant NCI/ADR-RES cells in the presence of 20μM MAD1 restored the potency of both Dox and Cis to a level

equivalent to the more sensitive OVCAR-3 cell line (**Fig. 9b**, analysis derived from combinatorial heat maps shown in Suppl. Fig. 9). Conversely, Paclitaxel showed only a modest improvement in potency when combined with 20μM MAD1 (**Suppl. Fig. 10**).

Clinically, late-stage epithelial ovarian cancer (EOC) is characterized by dissemination of the disease into the peritoneal cavity to form tumor spheroids, which is then typically treated with platinum-based chemotherapy (e.g. cisplatin).[87] In order to mimic these conditions ex vivo, ultra-low attachment culture plates were used to induce the formation of 3D tumor spheroids using OVCAR-3 cells, as well as three patient-derived lines (EOC15, 17, 19), which were then treated alone or in combination with cisplatin and/or MAD1 (**Fig 9c-f**). Remarkably, all three patient-derived tumor cell spheroids showed minimal reduction in size when treated with either cisplatin or MAD1 alone, while the combination produced potent and synergistic anticancer effects. These ex vivo studies confirm that MAD1 synergizes with platinum-based drugs to decrease ovarian cancer cell size, even in advanced patient-derived carcinomas that are often refractory to the standard of care.

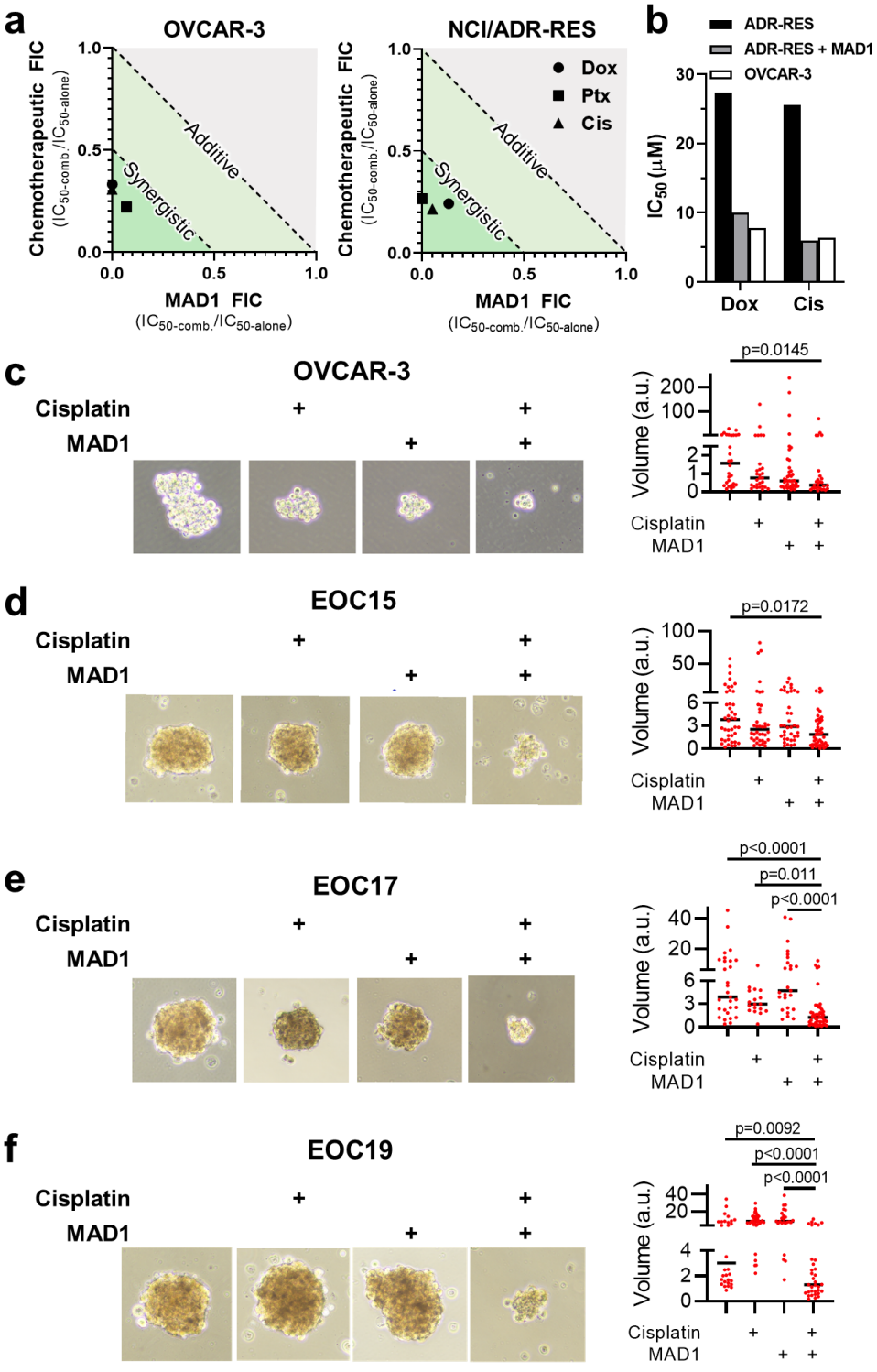

Figure 9. Peptide chemotherapeutic synergy. (**a**) Isobolograms of MAD1 and Doxorubicin (Dox), Paclitaxel (Ptx) or Cisplatin (Cis) combinatorial synergy in OVCAR-3 (*left*) and MCI/ADR-RES (*right*) cell lines. Fractional inhibitory concentration (FIC) <1 and <0.5 represent additive and synergistic effects, respectively. (**b**) Comparison of Dox and Cis IC_{50} towards NCI/ADR-RES, NCI/ADR-RES cells co-treated with 20μM MAD1, or the pre-resistant OVCAR-3 line. (**c-f**) Indicated ovarian cancer cell line or patient-derived ovarian carcinoma cells were cultured in ultra-low attachment conditions and treated for 48 hours with 2μM cisplatin or 4μM MAD1 alone and in combination. Data represent volume in arbitrary units (a.u.) and median.

Lipopeptisomes: Anticancer Peptide-Assembled Particles for Fusolytic Oncotherapy

LP Design, Formulation, and Characterization

To design LPs we selected three ACPs reported to possess potent oncolytic activity (IC50 < 15 μM), namely A4K14-Citropin 1.1, Halictine-2/11 and Lasioglossin-III (**Table 4**). For simplicity, the peptides will be hereafter referred to as Citropin, Halictine and Lasioglossin. These sequences, which were discovered in amphibian secretions and bee venoms, were initially characterized as broad spectrum antimicrobials before later discovery of their anticancer properties.[62,63,88] In the case of Citropin and Halictine, the sequences have undergone further optimization to yield engineered analogues (e.g. A4K14-citropin 1.1, Halictine-2/11) with enhanced oncolytic potency.[62,63] In both prokaryotic and eukaryotic cells, these peptides elicit their toxic action primarily by binding to the negatively charged cell membrane and partitioning into the lipid bilayer.[62,63,88,89] Subsequent folding into amphipathic α-helical conformations and self-assembly of the peptides leads to cell death via the formation of lytic pores, or through the solubilization of membrane constituents in a detergent-like fashion.[30,35,88,90]

Table 4. Sequence, physicochemical properties and reference for selected ACPs utilized to prepare LPs

Peptide	Sequence[a]	# AA	Formal Charge[b]	Ref.
A4K14-citropin 1.1	GLFAVIKKVASVIKGL-NH_2	16	+4	12
Halictine-2/11	GKWLSLLKHILK-NH_2	12	+5	13
Lasioglossin-III	VNWKKILGKIIKVVK-NH_2	15	+6	13

[a]All peptides are prepared with amidated C-terminus; [b]Formal charge includes N-terminal amin Histidine considered partially protonated for purposes of formal charge calculation.

Despite their significant therapeutic potential, all three of these sequences suffer from low therapeutic indices due to significant off-target hemolysis. Thus, these peptides serve as ideal models to test the potential for LPs to enhance the therapeutic utility of previously toxic ACPs. Conveniently, the selected peptides also possess varied amino acid composition, sequence length and formal charge (see Table 4), and therefore can be used to assess the potential of LPs to tolerate loading of peptide cargoes with diverse physicochemical properties.

To prepare LP particles, we incubated ACPs at various concentrations with ~150 nm liposomes, leading to direct interpolation of the peptides within the lipid nanoparticle bilayer. Importantly, the liposomal carrier is formed using a 1:1 molar ratio of phosphatidylcholine (PC) and phosphatidylserine (PS). This formulation mimics the aberrant lipid composition of the cancer cell membrane,[66] which is characterized by increased presentation of anionic PS lipids at the outer leaflet.[59,61] We, and others, have shown that this high density of PS imparts an electronegative surface potential that triggers the selective binding and folding of cationic ACPs into their bioactive lytic states.[52,53,66,91,92]

Using dynamic light scattering (DLS), we measured the influence of increasing amounts of loaded peptide on LP stability, expressed as a peptide:lipid ratio. **Fig. 10A** shows that LPs remain stable up to ratios of 0.04:1 to 0.2:1, dependent on the sequence employed. Representative particle size distribution plots for blank liposomes and the three LP formulations can be found in **Suppl. Fig. 55**. Increasing the ACP concentration beyond this failure threshold destabilized the lipid bilayer and led to particle rupture, as indicated by the complete loss of DLS signal. This suggests that the failed particles disassociate into ultrafine fragments not detectable by the light scattering instrument (<5nm). Importantly, given the propensity of these ACPs to lyse lipid membranes, the ability of LPs to support relatively high peptide:lipid ratios is surprising. For example, we found that Citropin formulations can be loaded with up to ~30 wt% of peptide, indicating that under these conditions integrated ACPs make up nearly a third of the LP particle by weight.

To better understand what drives this proficient loading of ACPs into the lipid carrier, we examined the influence of peptide physicochemical properties on LP stability. This was done by plotting the LP failure ratio, or the peptide:lipid threshold at which particle integrity is lost, against various sequence parameters, including peptide length, percentage of hydrophobic or basic residues, and formal charge. Results in **Fig. 10B** show a linear relationship between LP failure ratio and both peptide length and sequence hydrophobicity. No significant correlation with peptide formal charge, as well as percentage of basic residues in the ACP sequence, was observed (**Suppl. Fig. 16**). Taken together, this suggests that maximal

loading of ACPs into the particle lamella is largely dependent on the lipophilic nature of the peptide, as well as the number of amino acids in its sequence. The latter likely results from the ability for longer helical peptides (>13 residues) to more stably insert into fluid lipid membranes and span the bilayer thickness (~44Å) as a transmembrane helix.[93,94]

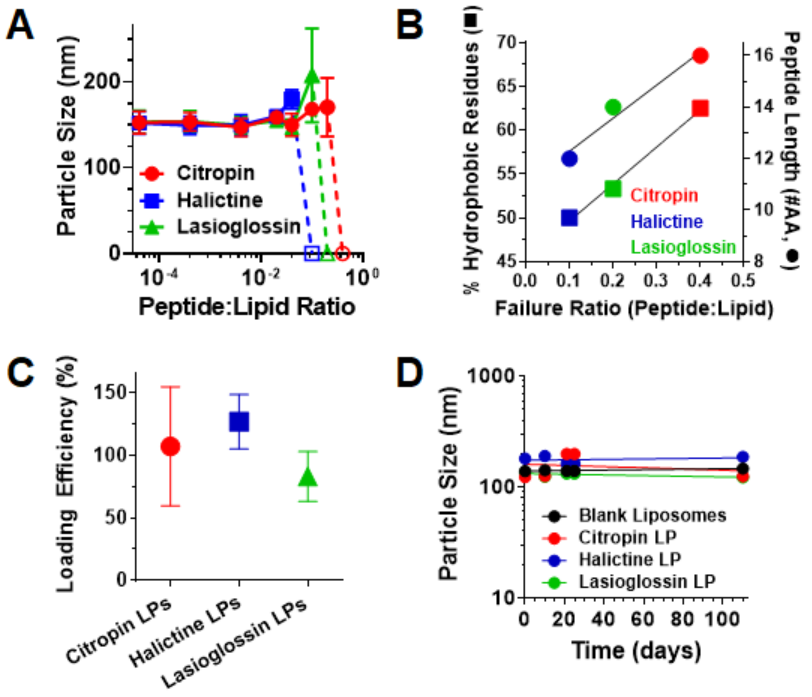

Figure 10. Preparation and physicochemical characterization of LPs. **(A)** Change in LP particle size as a function of increasing peptide:lipid ratio. Dashed line and open symbols indicate particle failure, as defined by the loss of DLS signal. **(B)** Change in the LP peptide:lipid failure ratio as a function of ACP hydrophobicity (% hydrophobic residues in the sequence; ■) or peptide length (number of amino acids; ●). **(C)** Percentage loading efficiency of each ACP into the final LP formulation. **(D)** Stability of LP particles, or the blank liposomal carrier, during long term-storage in buffer at room temperature. Particle stability was measured via DLS.

From these loading experiments we selected a peptide:lipid ratio of 0.02:1, representing 100 μM equivalent peptide, to prepare LPs for further studies as this produced stable formulations for all three ACPs tested. Cryo-TEM imaging of LPs, or the unloaded liposomal carrier as a control, showed no discernable change in particle morphology following integration of ACPs into the bilayer (**Suppl. Fig. 17**). To assess loading efficiency, we prepared LPs with each peptide, purified the particles via dialysis to remove unincorporated ACPs, and performed UV-Vis spectroscopy to measure the concentration of incorporated peptide. In the case of Halictine and Lasioglossin, their efficient integration into the carrier was evidenced by the emergence of a broad peak at 280 nm, reflecting the characteristic absorption maxima of tryptophan

residues in the loaded ACP (**Suppl. Fig. 18**). Calculating peptide concentration shows that Citropin and Halictine achieve quantitative loading into LPs of ~100%, while Lasioglossin shows an average efficiency of 83% (**Fig. 10C**). Finally, all three LP formulations were found to be stable when stored in buffer for over 100 days (**Fig. 10D**).

Next, utilizing giant unilamellar vesicles as a model membrane, we performed fluorescent confocal microscopy to study the localization of ACPs when loaded into the lipid carrier. This is important as effective delivery of ACPs into the cancer cell membrane during LP fusion requires incorporated peptides to be resident within the lipid corona, rather than adsorbed to the particle surface or dispersed within the solvent core. Images in **Fig. 11A** show that fluorescently-labeled Lasioglossin rapidly integrates into the vesicular lipid bilayer and spans the unilamellar membrane, reaching maximum incorporation within 3.5 minutes of addition (**Fig. 11B**). Circular dichroism spectroscopy demonstrates that all three ACPs remain disordered in physiologic buffer before particle binding, but display a strong α-helical signal characterized by minima in mean residue ellipticity at 208nm and 222nm upon incorporation within the negatively-charged liposomal carrier (**Fig. 11C, Suppl. Fig. 19**). Taken together, these results confirm that ACPs rapidly integrate across the lipid bilayer to prepare LPs, and in doing so pre-fold into α-helical conformations that are essential for their cytotoxic activity.[88,89,95]

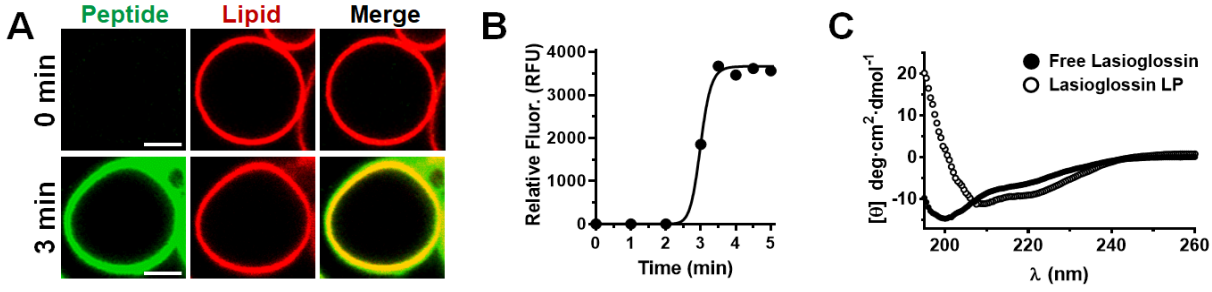

Figure 11. ACP localization and folding within the LP carrier. **(A)** Fluorescent confocal microscopy images of giant unilamellar vesicles (GUVs) showing the integration of fluorescein-labeled Lasioglossin (green) before (0 min.) and 3 min. after addition of the peptide (scale bar = 5 μm). GUVs were prepared at a 30:40:30 ratio of PS:PC:PE lipids, with 0.5 mol% of rhodamine-labeled PE included to aid in visualization (red). Merged image shows co-localization of peptide and lipid fluorescent signals. **(B)** Quantification of Lasioglossin fluorescence (in relative fluorescence units, RFU) at the GUV membrane as a function of time. **(C)** Circular dichroism spectrum demonstrating that Lasioglossin remains unfolded in physiologic buffer (●), but adopts an α-helical conformation when integrated into the negatively-charged lipid carrier to form LPs (○). CD spectrum of Citropin and Halictine LPs shown in Suppl. Fig. 19.

Membrane Fusion and Anticancer Activity of LPs

The preferential anticancer activity of free ACPs or peptide-loaded LP formulations was evaluated via the MTT assay following a 72 hour incubation with A549 lung carcinoma or HeLa cervical cancer cells, as well as non-cancerous HUVECs (human umbilical vein endothelial cells) as a control (**Fig. 12**). These studies test the ability of LPs to selectively deliver ACP cargo to cancer cells without influencing its lytic activity once integrated into the membrane. If the lipid carrier is inert and able to efficiently deliver the payload into tumor cells, we would expect a similar activity of ACP-loaded LPs with the corresponding free peptide. Gratifyingly, treatment of both A549 and HeLa cancer cell lines with all three LP formulations resulted in potent cytotoxic activity (IC50 = 1.0 – 5.2 μM), which is on the order of the free peptides (IC50 = 1.3 – 5.1 μM).

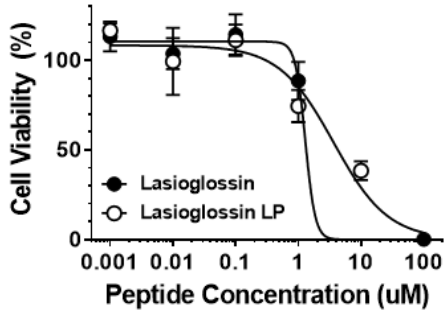

Treatment	IC_{50} (μM) A549	HeLa	HUVEC
Citropin	**4.8** ± 1.8	**2.2** ± 0.3	**6.4** ± 2.2
Citropin LP	**5.2** ± 1.7	**3.3** ± 0.5	**>50**
Halictine	**5.1** ± 1.6	**2.0** ± 0.4	**21.6** ± 2.4
Halictine LP	**5.2** ± 3.4	**2.3** ± 0.2	**>50**
Lasioglossin	**1.3** ± 2.5	**1.3** ± 1.2	**29.6** ± 3.0
Lasioglossin LP	**1.0** ± 1.3	**3.8** ± 0.9	**>50**

Figure 12. (*Top*) Representative cytotoxicity profile of free Lasioglossin and the corresponding LP formulation against HeLa (cervical carcinoma) cells. (*Bottom*) Tabulated IC_{50} values ± standard deviation for each ACP and its corresponding LP particle formulation after a 72h incubation with A549 (lung carcinoma) and HeLa cancer cell lines, or non-cancerous HUVECs (human umbilical vein endothelial cell) as a control.

Conversely, we observed a notable reduction in the off-target toxicity of ACPs towards healthy HUVEC controls when peptides are loaded into the LP carrier. In fact, we were unable to calculate exact

IC_{50} values for the particles as we did not observe any significant loss of HUVEC viability, even at the highest peptide loading concentration tested (50 μM). In the case of Citropin, toxicity of this peptide towards HUVECs is reduced by nearly an order of magnitude when delivered by LPs. This improvement in ACP specificity when formulated into an LP particle may be due to a reduced potential for fusion of the lipidic carrier with the healthy mammalian cell membrane, relative to tumor cells. The outer leaflet of non-cancerous cells is characterized by high PC content,[56,57] which is a lipid whose headgroup strongly binds water to establish a lipid-water interface that prevents contact-mediated fusion with nearby bilayers.[96] Further, the surfaces of healthy mammalian cells are scarce of PS lipids,[56,57] which are abundant on the outer leaflet of cancer cells due to the aberrant function of enzymes responsible for maintaining proper lipid asymmetry in malignant phenotypes.[59–61] Relevant to the function of LP particles, PS is a key mediator of membrane fusion due to its ability to bind divalent Ca2+ cations that are responsible for removing water from the lipid interface.[96,97] Taken together, these results strongly support the ability of LPs to preferentially fuse with tumor cells and successfully integrate the lytic ACP payload into the membrane, while circumventing off-target toxicity of the peptide cargo towards healthy tissues.

To further test this assertion, as well as directly visualize LP integration and ACP assembly within tumor cell membranes, we performed confocal microscopy employing dual-labeled LP formulations. Here, the liposomal carrier and loaded ACP were independently labeled with rhodamine and fluorescein fluorophores, respectively, to visualize subcellular localization of each component upon LP-membrane fusion (**Fig. 13**). Fluorescent microscopy images collected at 24 and 48 hours (**Suppl. Fig. 20** and **Fig. 13A**, respectively) show that the lipid carrier (red) is rapidly integrated into treated cancer cells and shows diffuse localization across the membrane and cytoplasmic compartments. Corresponding differential interference contrast (DIC) images of LP-incubated cells and untreated controls can be found in **Suppl. Fig. 21**. This extensive particle uptake likely results from the upregulation of pathways responsible for scavenging and internalizing exogenous lipids in cancer cells, a necessary requirement to meet the high metabolic demands of these rapidly proliferating cells.[98,99] Internalized lipids are subsequently processed through catabolic fatty

acid oxidation pathways and used to form new membrane constituents and signaling molecules, as well as to post-translationally modify proteins. This may explain the broad dissemination of the lipid signal observed following the assimilation of LPs into treated cancer cells at all tested time points.

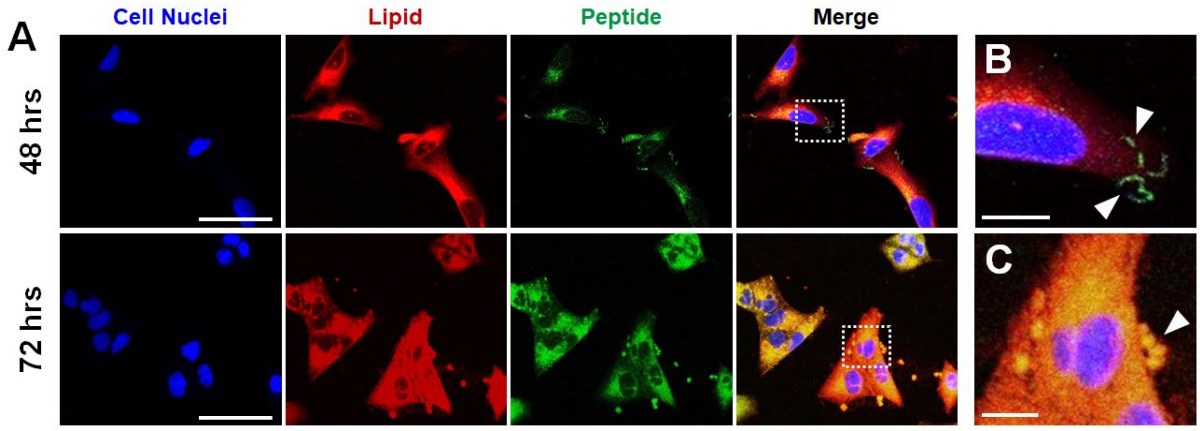

Figure 13. LP integration into cancer cells and subcellular tracking of delivered lipids (red) and ACPs (green). **(A)** Fluorescent confocal microscopy images of A549 lung carcinoma cells treated for 48 or 72 hours with Lasioglossin LPs (scale bar = 50 μm). Magnification of dotted regions in the 48 and 72 hour merged images are shown in panels B and C, respectively. **(B)** Assembly of LP-delivered Lasioglossin into fibrillary structures (white arrow) at the cancer cell surface (scale bar = 10 μm). **(C)** Nuclear fragmentation and membrane blebbing (white arrow) of A549 cells following a 72 hour incubation with labeled Lasioglossin LPs (scale bar = 10 μm).

Interestingly, delivered ACPs were localized predominantly to the cancer cell surface as assemblies of micron-sized proto-fibrils at 24 and 48 hours of incubation (Suppl. Fig. 20 and **Fig. 13B**). To our knowledge, this is the first time higher ordered ACP structures have been resolved by confocal microscopy following peptide self-assembly within cancer cell membranes. We also found that a portion of delivered ACPs are transported intracellularly, appearing as diffuse fluorescence within the cytoplasm of treated cells. This is particularly evident at 72 hours of incubation (Fig. 13A, lower panels). Together this suggests that at early time points much of the delivered ACP cargo self-associates in the cancer cell membrane to form higher ordered lytic structures, followed later by shuttling of the peptides to endosomal and cytoplasmic intracellular compartments during membrane turnover. Based on these observations, we cannot rule out the fact that intracellularly delivered ACPs may be able to permeabilize mitochondrial membranes inside cells and induce apoptosis. This is supported by the representative image shown in **Fig. 13C,** which indicates that at 72 hours LP-treated cancer cells begin to display fragmented nuclei and undergo membrane

destabilization, as indicated by lipid blebbing at the cell surface (see white arrows in Fig. 13C). Hence, LPs may kill cancer cells through combinatorial mechanisms that include both physical membrane lysis and induction of apoptotic pathways.

Hemolytic Activity of LP Particles

We next studied the cytotoxic selectively of LPs with respect to their ability to lyse tumor cells versus healthy human erythrocytes. Like all mammalian cells, the surface of red blood cells (RBCs) are composed largely of cholesterol and various phospholipids that are asymmetrically separated across an inner and outer leaflet.[58] Previous studies have shown that the presence of negatively charged lipids, such as phosphatidylethanolamine, on the outer leaflet of red blood cells potentiates the off-target binding of ACPs to their surfaces and leads to hemolysis, with lytic potency generally associated with peptide hydrophobicity and helicity.[100] To assess potential reduction in ACP hemolytic toxicity when loaded into the LP carrier, we first measured the integrity of RBCs following a 24 hour incubation with each ACP at a representative low (10 μM) and high (100 μM) peptide concentration (**Fig. 14**). Not surprisingly, under these conditions we observed moderate (18% – 36%) hemolysis at the low ACP concentration tested, and complete destruction of RBCs at 100 μM of peptide (Fig. 8, left). Remarkably, the toxicity of these sequences was reduced by nearly two orders of magnitude when incorporated within LPs. For example, all three LP formulations showed ≤8% hemolysis at the highest tested concentration of loaded ACP (100 μM). In fact, under these stringent incubation conditions both Citropin and Halictine LP formulations elicited <5% total hemolysis, which is the threshold at which materials are considered non-hemolytic by ASTM guidelines (see protocol ASTM-F756).

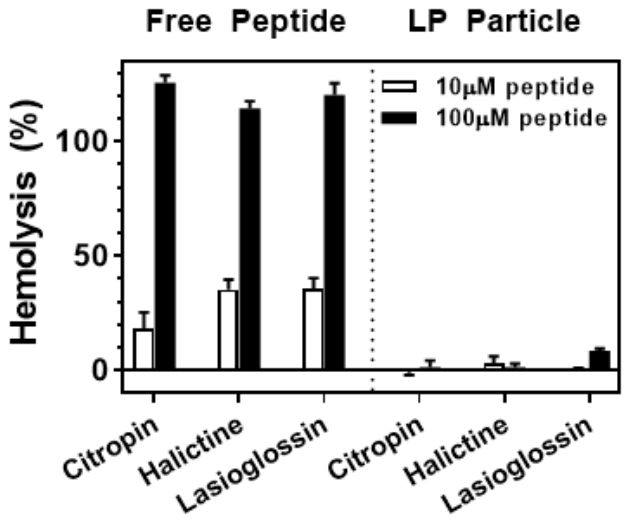

Figure 14. Percentage hemolysis of human RBCs following a 24h incubation with (*Left*) free Citropin, Halictine and Lasioglossin ACPs, or the (*Right*) corresponding LP particle formulation. Hemolytic activity for each treatment condition tested is shown at a low (10 μM, white bar) or high (100 μM, black bar) concentration of equivalent peptide. Data is normalized to untreated hRBCs, and percent hemolysis calculated relative to positive controls lysed with Triton-X.

From this data we can calculate an approximate therapeutic index (the ratio of therapeutic vs. toxic dose) for each LP formulation by dividing the hemolytic threshold (~100 μM) by the average IC_{50} value for each particle towards cancer cells (Fig. 12). This analysis reveals that LP particles possess a therapeutic index of 24, 27 and 42 for Citropin, Halictine and Lasioglossin formulations, respectively. Gratifyingly, all three of these LP formulations are characterized by therapeutic indices amenable to clinical application, being well above that of most chemotherapeutic agents.[101]

This significant reduction in the hemolytic potential of ACPs when incorporated within the LP carrier may be a result of the unique composition of the RBC surface. First, erythrocytes lack the lipid scavenging receptors displayed on other mammalian cell types, and which are particularly abundant on cancer cells.[98,99,102] This suggests that LPs may be poorly recruited to the surfaces of RBCs and thus limited in their ability to fuse to the membrane and integrate the lytic ACP payload. Second, the vast majority of PS content in the healthy RBC bilayer is confined to the inner leaflet in order to prevent premature clearance by immune cells.[58,103] Relevant to the activity of our LP particles, PS is a key mediator of membrane fusion due to its ability to bind divalent Ca^{2+} cations that are responsible for removing water from the lipid interface.[96,97] This ultimately allows more intimate contact between dehydrated bilayers and the nucleation

of lamellar defects that are a pre-requisite for initiation of membrane fusion. In addition to this distinct lack of PS, the outer monolayer of RBCs is rich with PC lipids, which possess a headgroup that tightly binds to water and as a result potently inhibits interbilayer fusion.[58,96] Taken together, this suggests that the compositional mismatch of lipids in our particles and the erythrocyte membrane may ultimately hinder LP fusion with RBCs, and instead shift their preferential interaction towards the PS-rich surface of cancer cells.[59–61]

Chapter 4
Conclusion and Future Work

Although AMPs have been extensively studied and developed as treatments for infectious diseases, their translation towards anticancer applications has been underexplored. Here, we demonstrate general design principles that can be used to re-purpose AMP scaffolds into cancer-specific host defense peptides. This approach eliminates the need for large empirical screens and, hence, allows for a robust and rapid ACP discovery pipeline. Unique to this strategy is that it can develop anticancer agents that do not target a resistance-susceptible biochemical pathway, but instead act by physically disrupting key structural elements, including the plasma and nuclear membrane, that are difficult for cancer cells to mutationally alter. As an exemplary application, we show that the tuberculosis-specific host defense peptide, MAD1, can be repurposed as a potent ovarian cancer targeting ACP. Surprisingly, this peptide displays an unusual specificity for human ovarian carcinomas and synergistically enhances the activity of clinical therapies towards drug-refractory and -resistant tumors. This is particularly impactful as many ovarian cancer patients are diagnosed at an advanced stage, and either relapse or succumb to the disease as a result of chemotherapeutic resistance. This suggests that ACPs engineered from AMP templates, which synergistically exploit lytic and apoptotic anticancer mechanisms, may be a unique and potentially transformative addition to combinatorial therapies against drug-resistant gynecological cancers.

In order to address some of the limitations inherent to anticancer peptides, I report the design and efficacy of fusolytic nano-scale particles prepared via the interpolation of membrane-active helical peptides into liposomal lamella. The resulting particles, referred to as lipopeptisomes, can be efficiently loaded with oncolytic ACPs and remain stable during long term storage. We show that incorporation of ACPs within LP particles did not disrupt or diminish their lytic behavior, leading to proficient assimilation of the peptides into cancer cells membranes and potent cytotoxicity profiles. Interestingly, when taken within the broader context of the biophysical mechanisms that mediate interbilayer fusion, our work provides new insights

into the potential to target nanoparticles to specific cell types via compositional matching of particle-cell lipid constituents.

With respect to the clinical utility of ACPs, this new delivery strategy is able to impart a significant improvement in the anticancer specificity of oncolytic peptides by reducing their off-target hemolytic potential and toxicity towards healthy, non-cancerous tissues. As a result, previously toxic ACPs are transformed into potential drug candidates that can be considered 'non-hemolytic' by ASTM guidelines and which possess clinically relevant therapeutic indices. In fact, LPs display therapeutic windows well above that of many clinically employed chemotherapeutics.[104] These nanomaterials even exceed the toxicity profile of some antibiotics, such as vancomycin (index ~ 10),[105] which are often considered the paragon class of therapeutics with which to benchmark biocompatibility.

It is worth noting that in our studies the tolerance of LPs was established based on their in vitro profile, and thus we cannot rule out the potential for secondary effects in vivo. However, the fact that hemolytic toxicity remains a key barrier to the clinical translation of many membrane-active peptides,[28] and combined with the low toxicity and immunogenicity profiles of lipid nanoparticles,[106] suggests that LPs represent a biocompatible delivery platform with significant potential to advance new oncolytic strategies in the clinic. Thus, we present a novel delivery modality poised to improve the utility of ACPs, open up new combinatorial approaches in oncology, and may add to our arsenal of strategies to combat the emergence of therapeutic resistance in precision medicine.

Appendix A

Supplemental Information

Supplemental Fig. 1. RP-HPLC and ESI-MS of MAD1

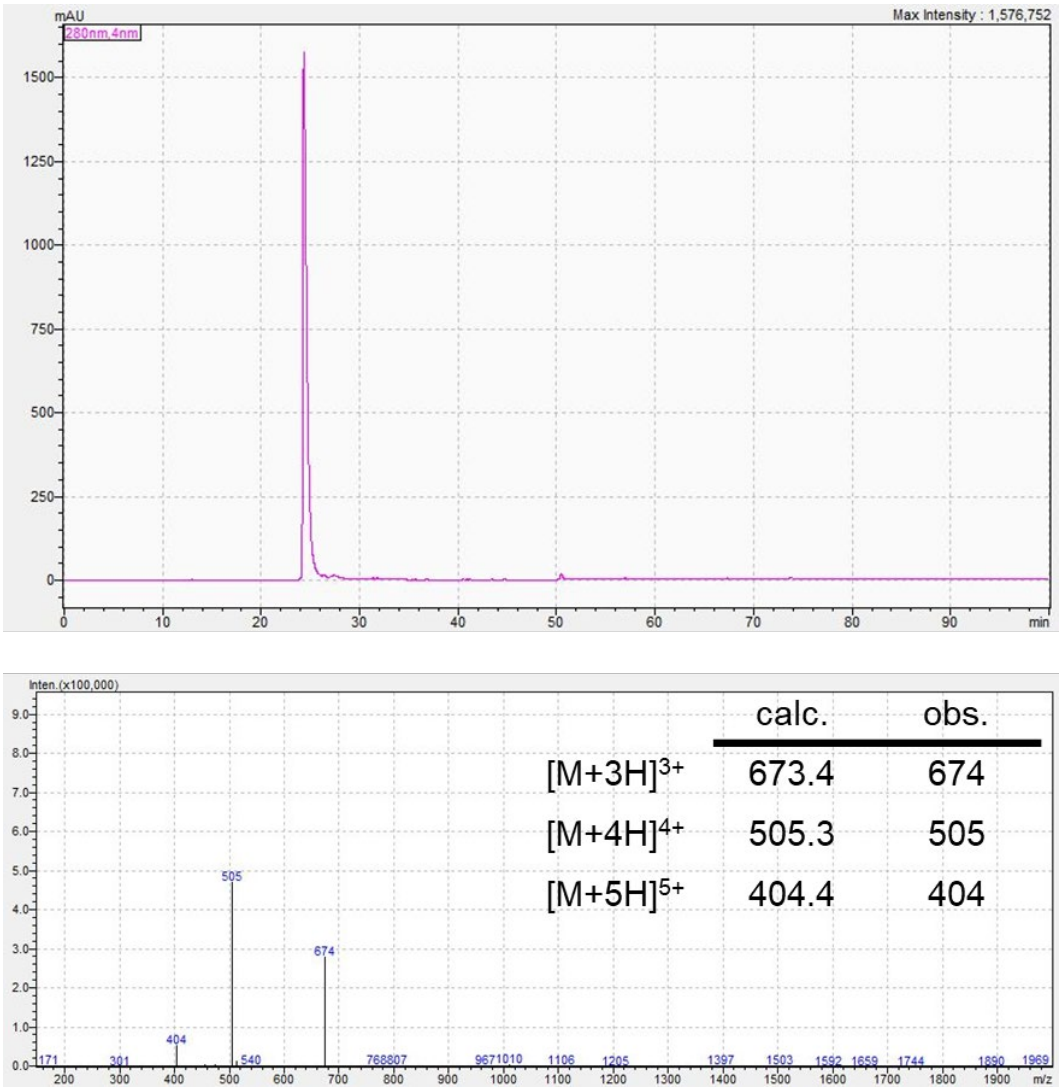

Figure 15. *Top:* Analytical HPLC chromatogram (Luna Omega C18 column, linear gradient of 0-100 % solvent B over 100 minutes) and *Bottom:* ESI (+) mass spectrum of purified MAD1 with calculated and observed masses reported.

Supplemental Fig. 2. RP-HPLC and ESI-MS of FITC-MAD1

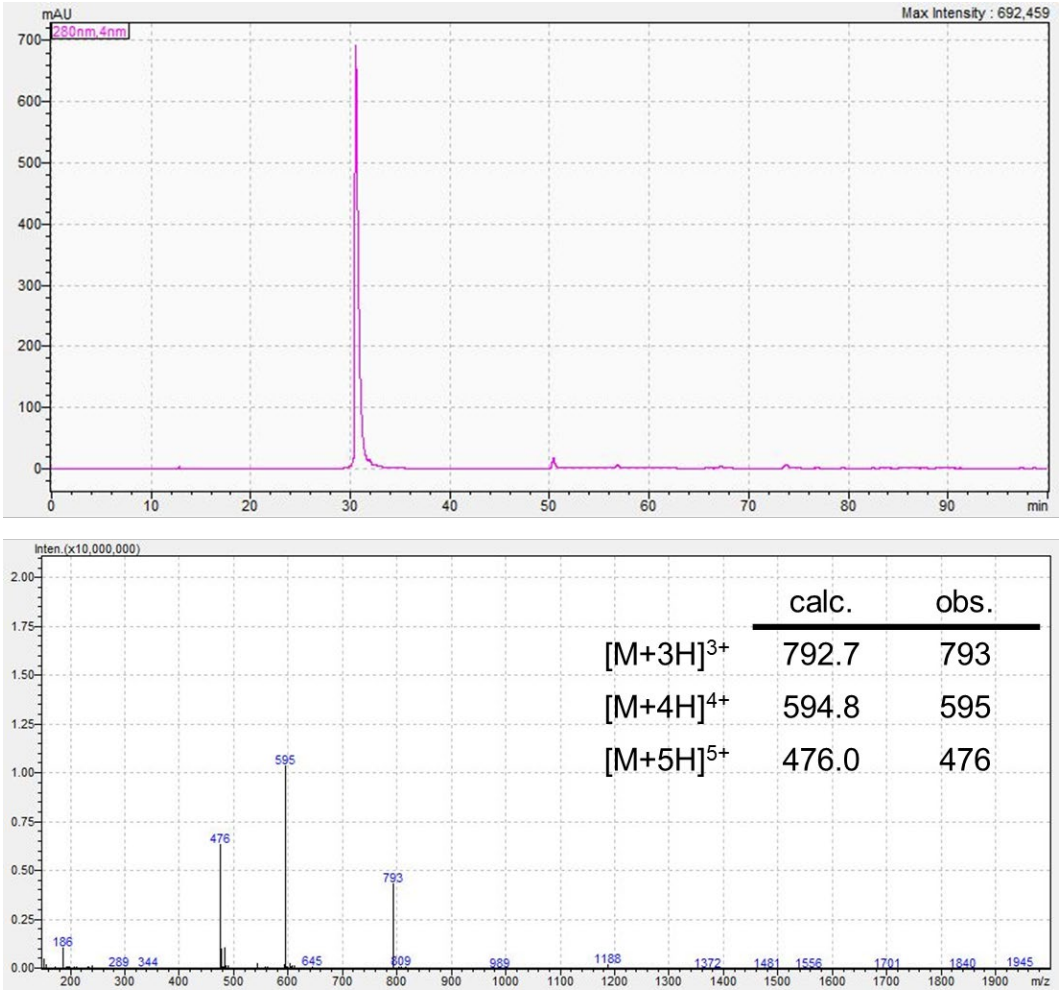

Figure 16. *Top:* Analytical HPLC chromatogram (Luna Omega C18 column, linear gradient of 0-100 % solvent B over 100 minutes) and *Bottom:* ESI (+) mass spectrum of purified FITC-MAD1 with calculated and observed masses reported.

Supplemental Fig. 3. RP-HPLC and ESI-MS of DAP1

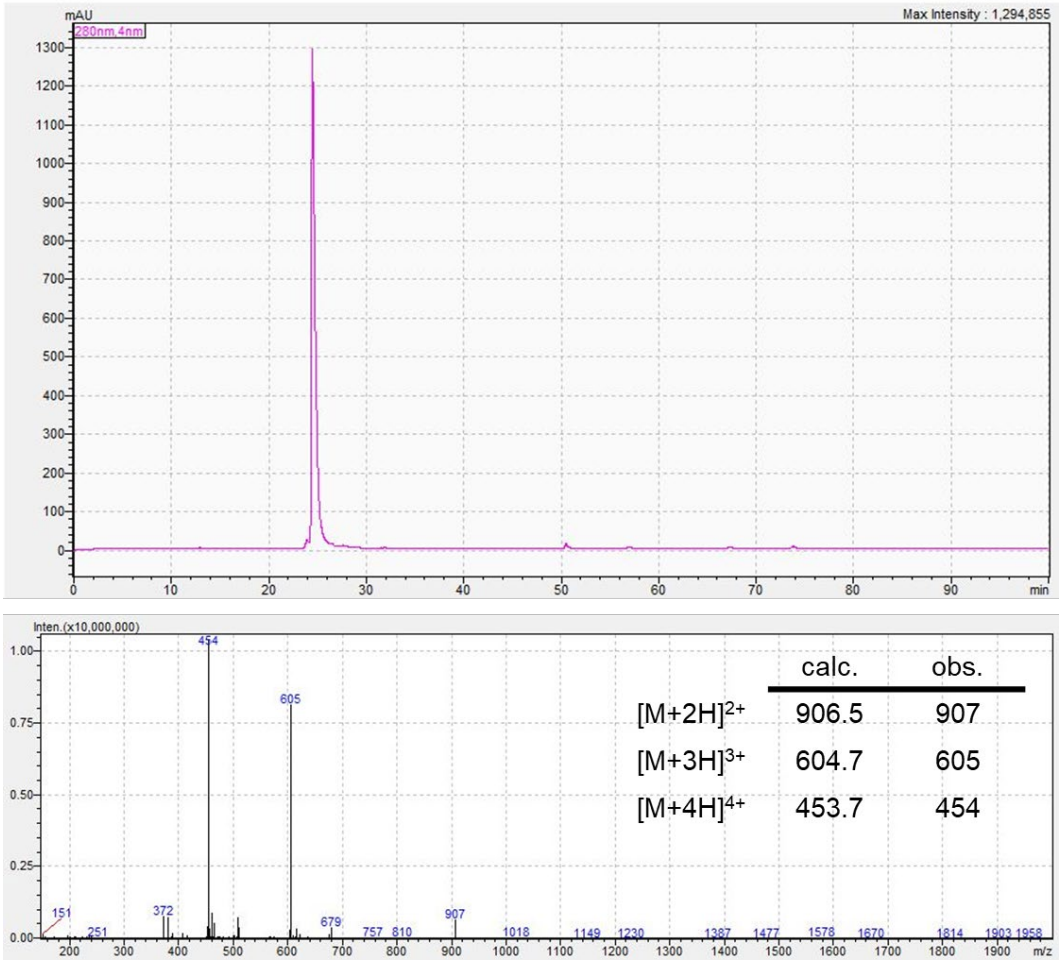

Figure 17. *Top:* Analytical HPLC chromatogram (Luna Omega C18 column, linear gradient of 0-100 % solvent B over 100 minutes) and *Bottom:* ESI (+) mass spectrum of purified DAP1 with calculated and observed masses reported.

Supplemental Fig. 4. RP-HPLC and ESI-MS of DAP2

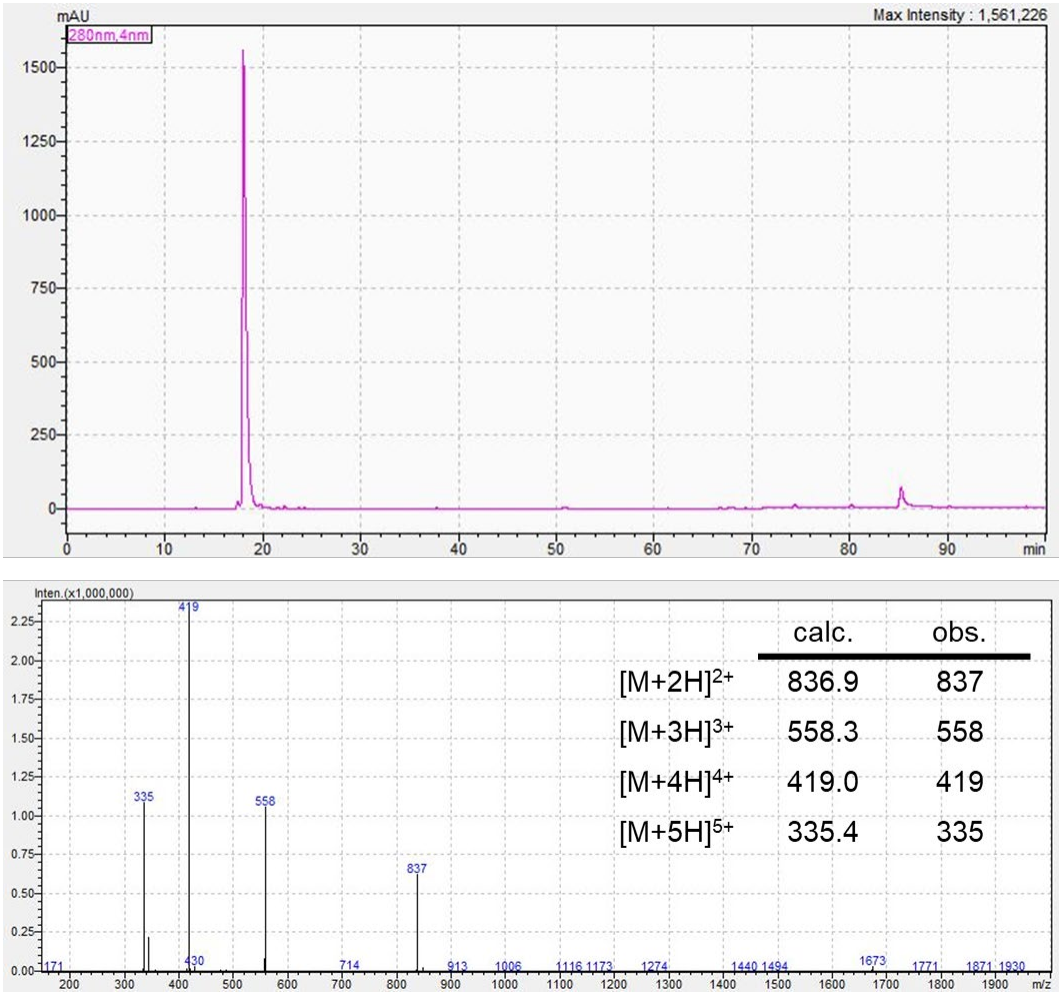

Figure 18. *Top:* Analytical HPLC chromatogram (Luna Omega C18 column, linear gradient of 0-100 % solvent B over 100 minutes) and *Bottom:* ESI (+) mass spectrum of purified DAP2 with calculated and observed masses reported.

Supplemental Fig. 5. Peptide cytotoxicity curves against tumor cell line panel

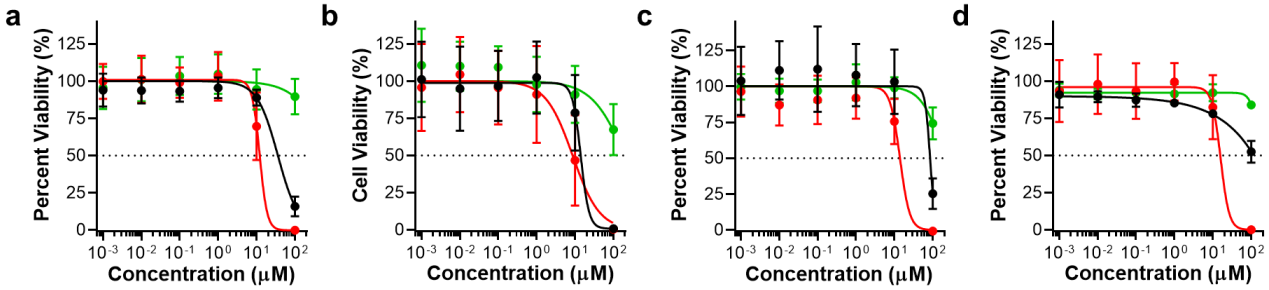

Figure 19. Cytotoxicity curves for MAD1 (black), DAP1 (red) and DAP2 (green) peptides against (**a**) A549 (lung carcinoma), (**b**) OVCAR-3 (ovarian carcinoma), (**c**) NCI/ADR-RES (drug-resistant ovarian carcinoma) and (**d**) T24 (urinary bladder transitional cell carcinoma) cells. Dashed line indicates IC_{50}.

Supplemental Fig. 6. Images of membrane disruption by ACPs

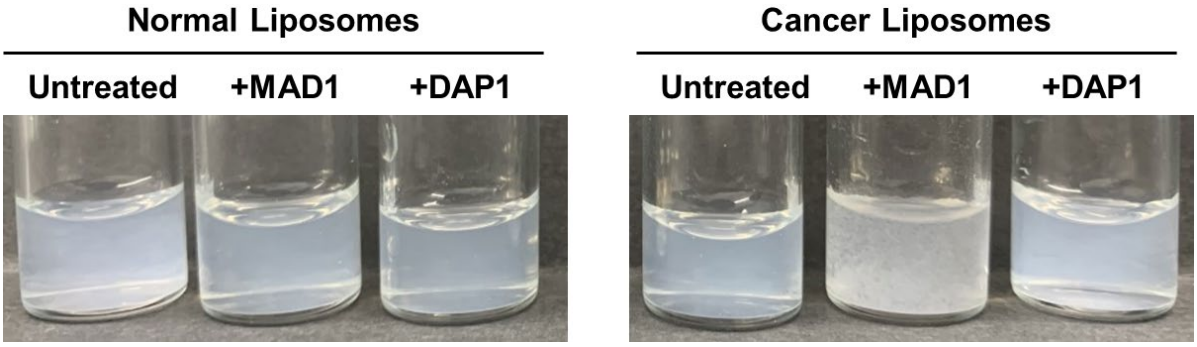

Figure 20. Images of normal (*left*) and cancer (*right*) membrane liposomal solutions before (untreated) and after treatment with either the MAD1 or DAP1 peptide. Formation of large flocculates in cancer liposomal solutions treated with MAD1 provides visual confirmation of selective membrane disruption.

Supplemental Fig. 7. SEM of untreated A549 cell

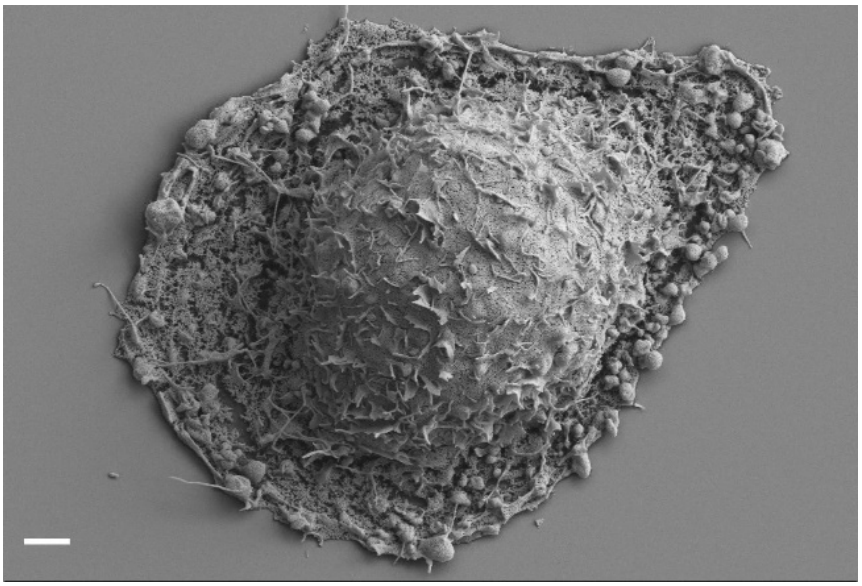

Figure 21. SEM image of untreated A549 cell. Scale bar = 5μm.

Supplemental Fig. 8. Flow cytometry histograms of TMRE-stained OVCAR-3 cells

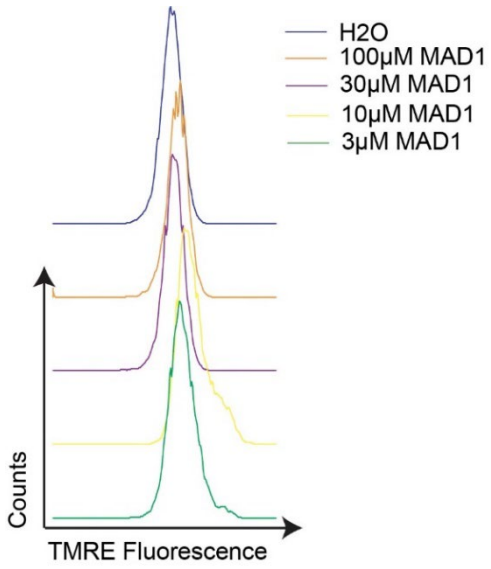

Figure 22. Flow cytometric analysis of OVCAR-3 cells labeled with TMRE and treated in the absence (H_2O) or presence of the MAD1 peptide at varying concentrations.

Supplemental Table 1. FIC of MAD1 and chemotherapeutics

Table 5. FIC of MAD1 and chemotherapeutics

	Combined FIC Score		
Cell Line	**Dox**	**Ptx**	**Cis**
OVCAR-3	0.33	0.30	0.31
NCI/ADR-RES	0.37	0.27	0.27

Supplemental Fig. 9. Combinatorial heat maps of MAD1-drug cytotoxicity

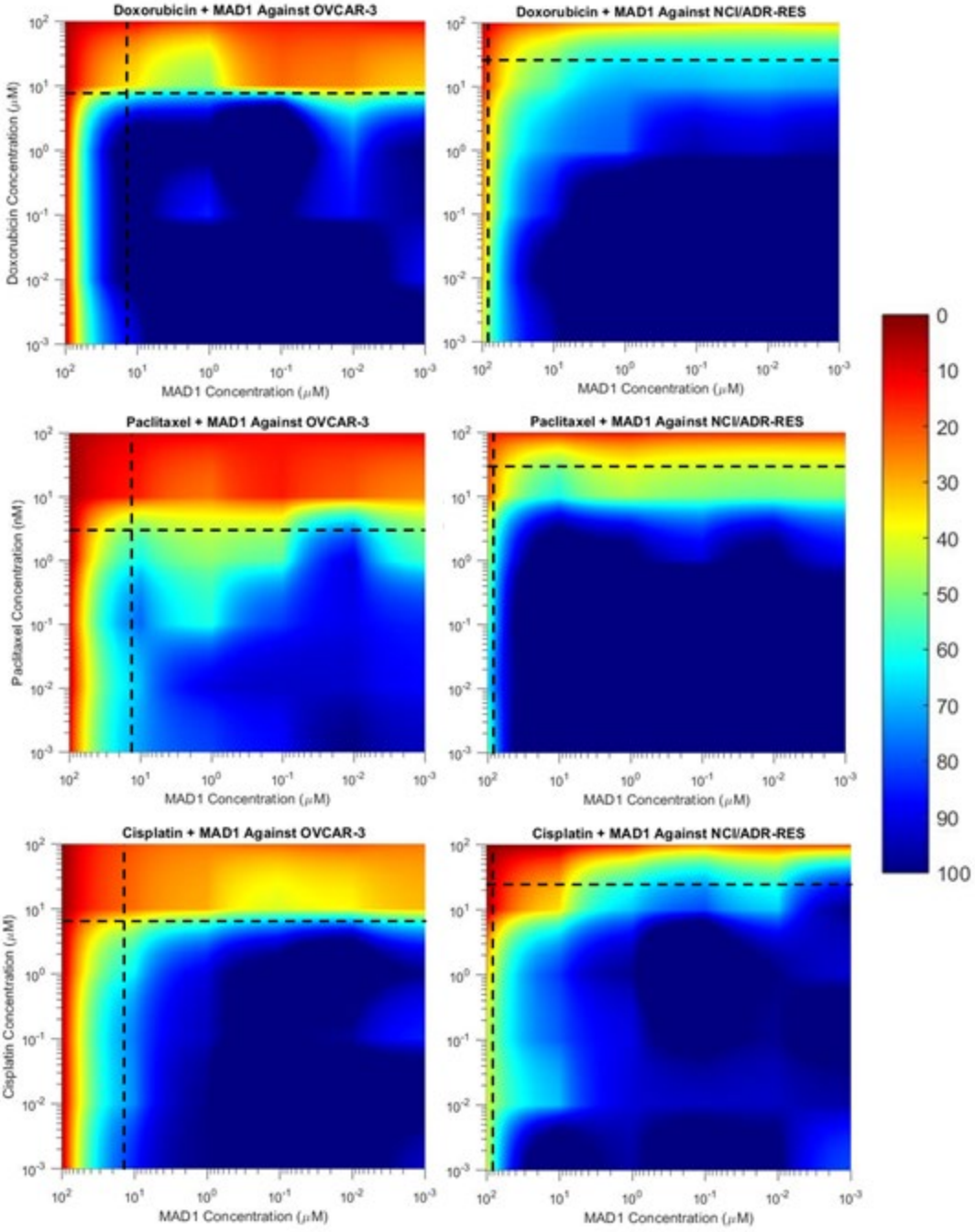

Figure 23. Heat map of MAD1 and listed drug combinatorial cytotoxicity towards OVCAR-3 and NCI/ADR-RES cell lines. Color legend represents 100% (blue) to 0% (red) cell viability. Dashed lines represent the individual IC_{50} of each compound in the tested cell line.

Supplemental Fig. 10. Comparison of Ptx activity with MAD1 co-treatment

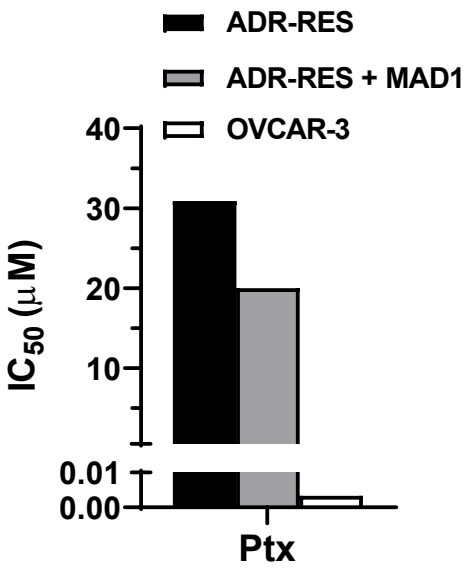

Figure 24. Comparison of Ptx IC_{50} towards NCI/ADR-RES, NCI/ADR-RES cells co-treated with 20μM MAD1, or the pre-resistant OVCAR-3 line.

Supplemental Fig. 11. RP-HPLC and ESI-MS of Citropin

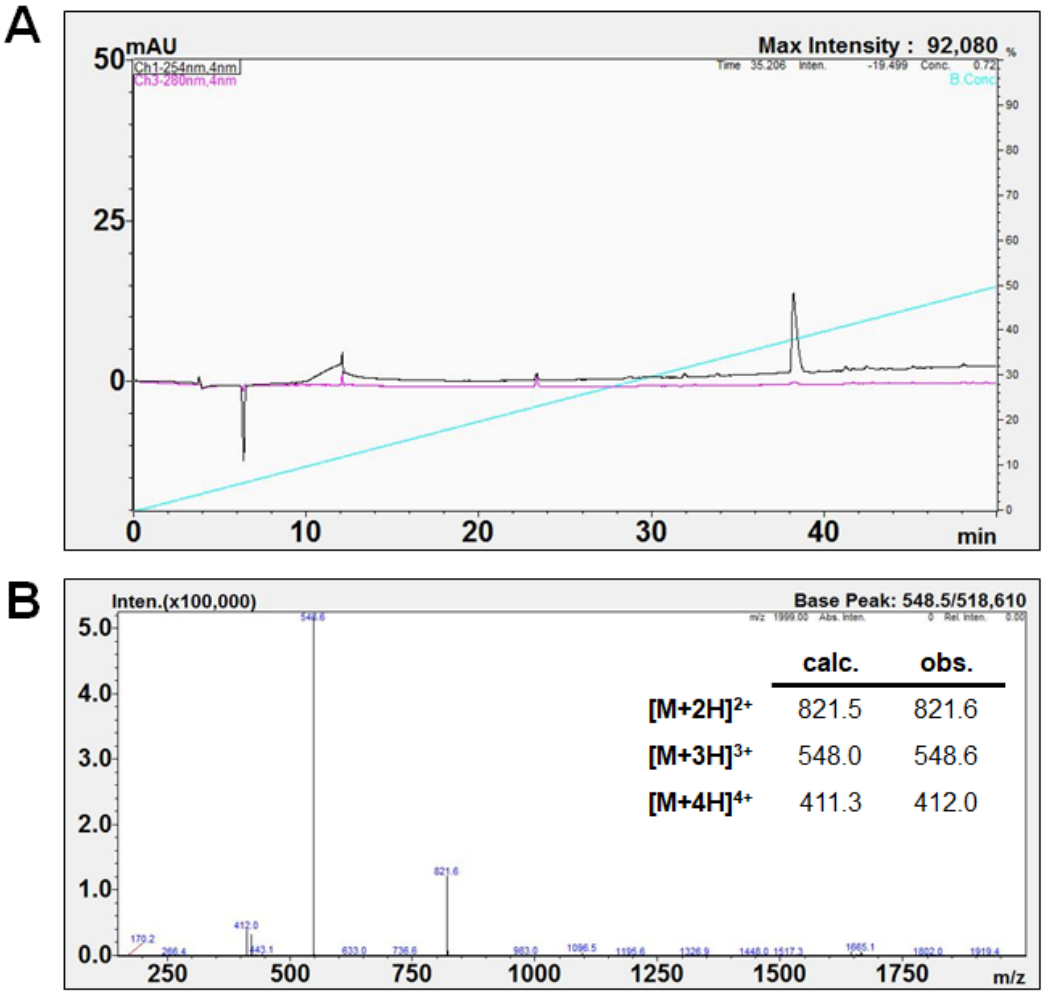

Figure 25. A) Analytical HPLC chromatogram (Luna Omega C18 column, linear gradient of 0-50 % solvent B over 50 minutes) and (**B**) ESI (+) mass spectrum of purified Citropin.

Supplemental Fig. 12. RP-HPLC and ESI-MS of Halictine

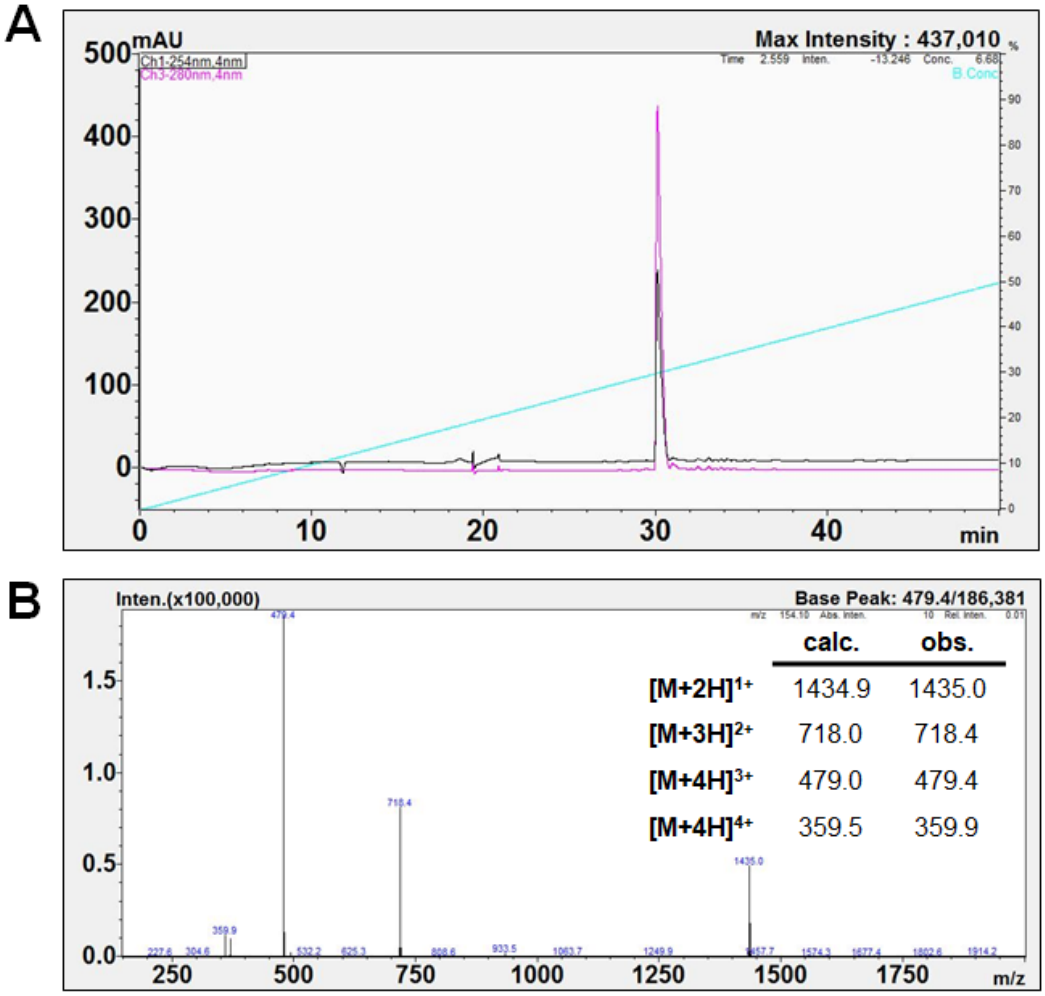

Figure 26. (**A**) Analytical HPLC chromatogram (Luna Omega C18 column, linear gradient of 0-50 % solvent B over 50 minutes) and (**B**) ESI (+) mass spectrum of purified Halictine.

Supplemental Fig. 13. RP-HPLC and ESI-MS of Lasioglossin

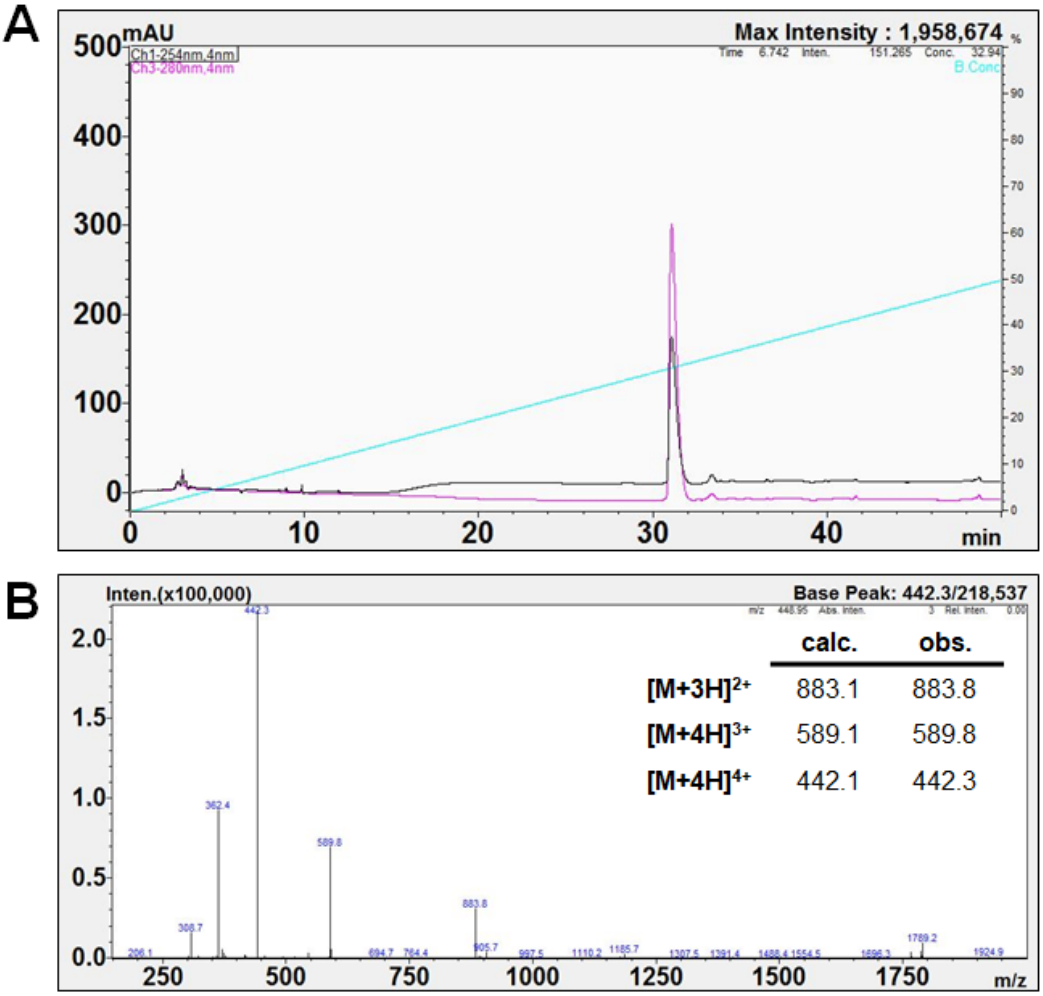

Figure 27. (**A**) Analytical HPLC chromatogram (Luna Omega C18 column, linear gradient of 0-50 % solvent B over 50 minutes) and (**B**) ESI (+) mass spectrum of purified Lasioglossin.

Supplemental Fig. 14. RP-HPLC and ESI-MS of fluorescently-labeled Lasioglossin

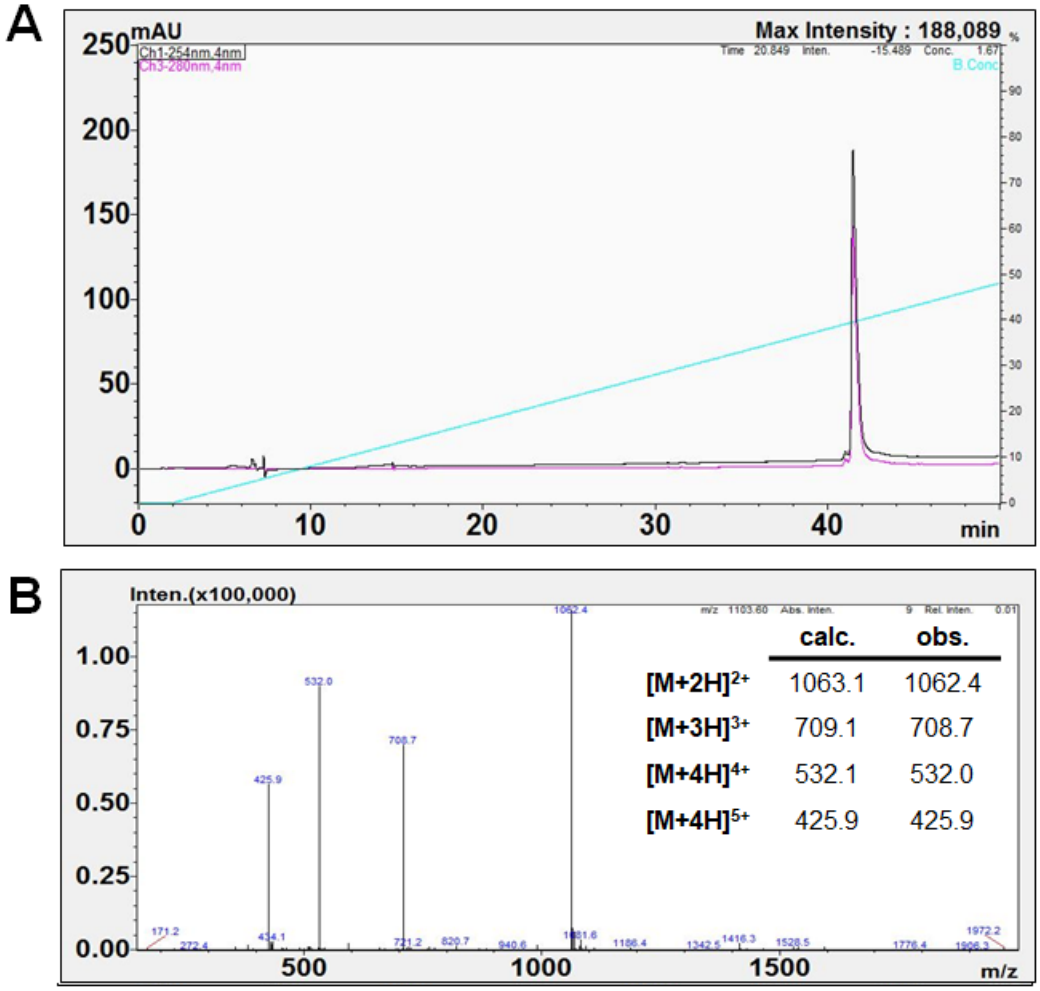

Figure 28. (**A**) Analytical HPLC chromatogram (Luna Omega C18 column, linear gradient of 0-50 % solvent B over 50 minutes) and (**B**) ESI (+) mass spectrum of purified fluorescein-labeled Lasioglossin.

Supplemental Fig. 15. Particle size distribution of the liposomal carrier and LP formulations

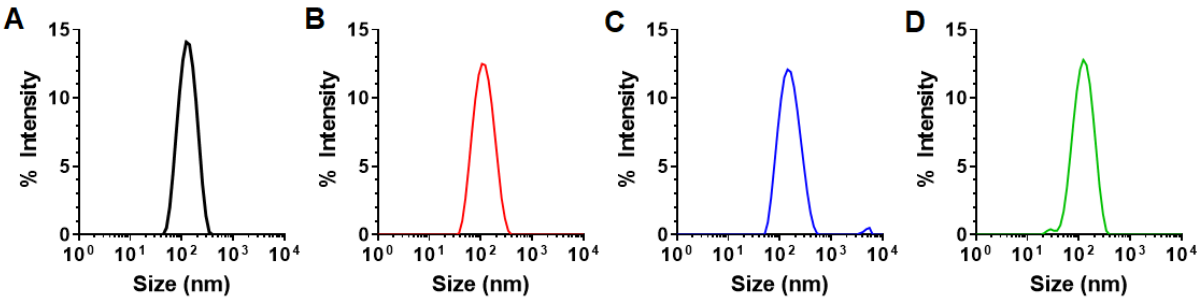

Figure 29. Particle size distribution of (**A**) the blank liposomal carrier (1:1 POPC:POPS), or (**B**) Citropin, (**C**) Halictine and (**D**) Lassioglossin loaded LPs (100 µM peptide), as measured by DLS.

Supplemental Fig. 16. Influence of peptide formal charge and relative basicity on LP stability

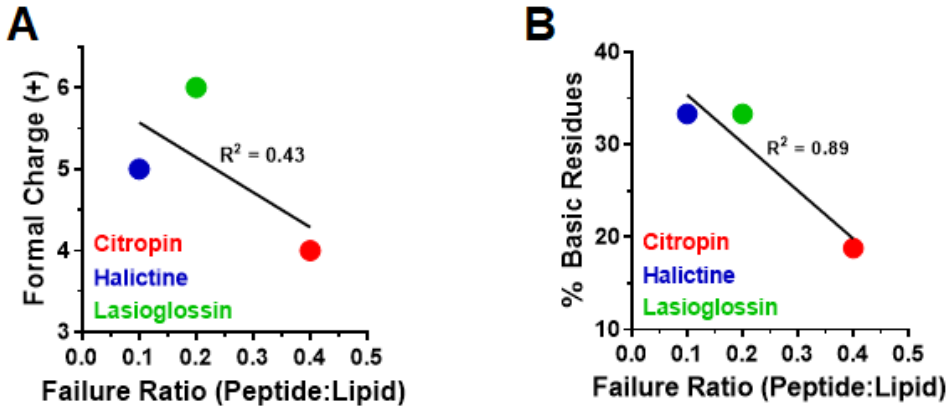

Figure 30. Change in the LP peptide:lipid failure ratio as a function of (**A**) peptide formal charge, or (**B**) Percentage of basic residues in the ACP sequence.

Supplemental Fig. 17. Cryo-TEM images of the liposomal carrier and LP formulations

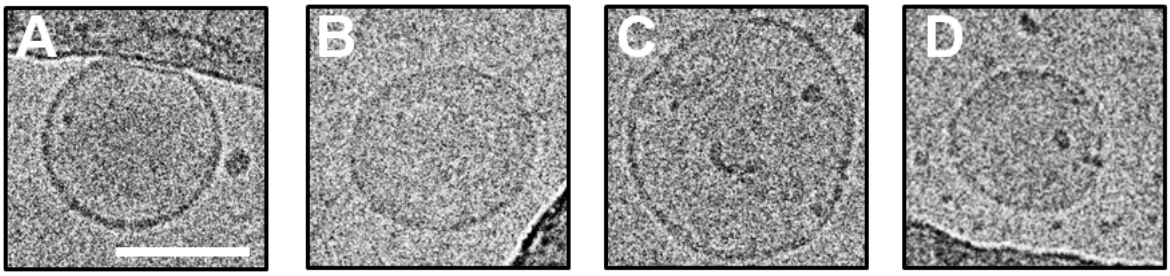

Figure 31. Cryo-TEM images of (**A**) the blank liposomal carrier (1:1 POPC:POPS), or (**B**) Citropin, (**C**) Halictine and (**D**) Lassioglossin loaded LPs (100 µM peptide). Scale bar = 100 nm.

Supplemental Fig. 18. UV spectrum of ACP-loaded LPs

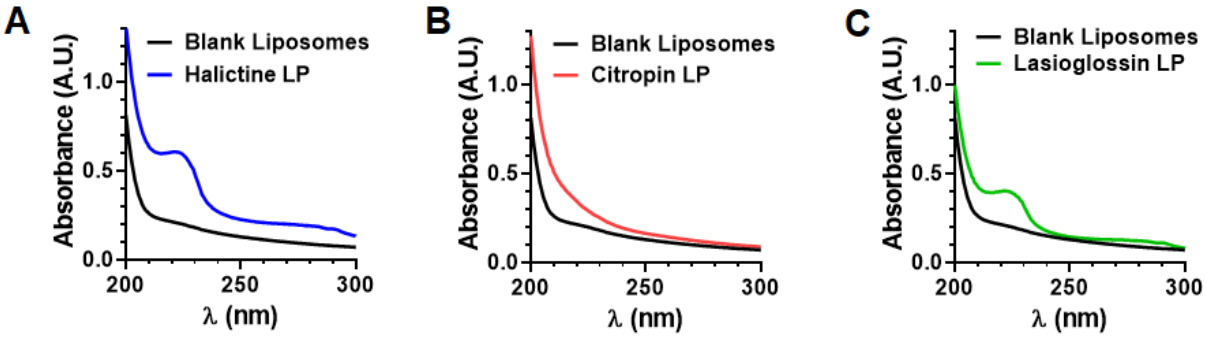

Figure 32. UV spectrum of ACP-loaded LPs or the blank liposomal carrier (black).

Supplemental Fig. 19. CD spectrum of Citropin- and Halictine-loaded LPs

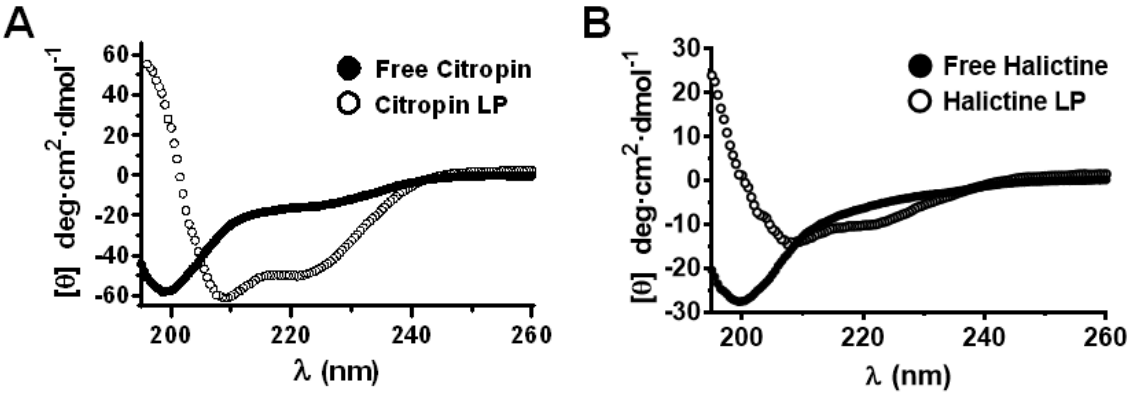

Figure 33. Circular dichroism (CD) spectrum of (**A**) Citropin or (**B**) Halictine peptides in physiologic buffer solution (●) or when integrated into the negatively-charged lipid carrier to form LPs (○).

Supplemental Fig. 20. Fluorescent microscopy of Lasioglossin LP treated cells

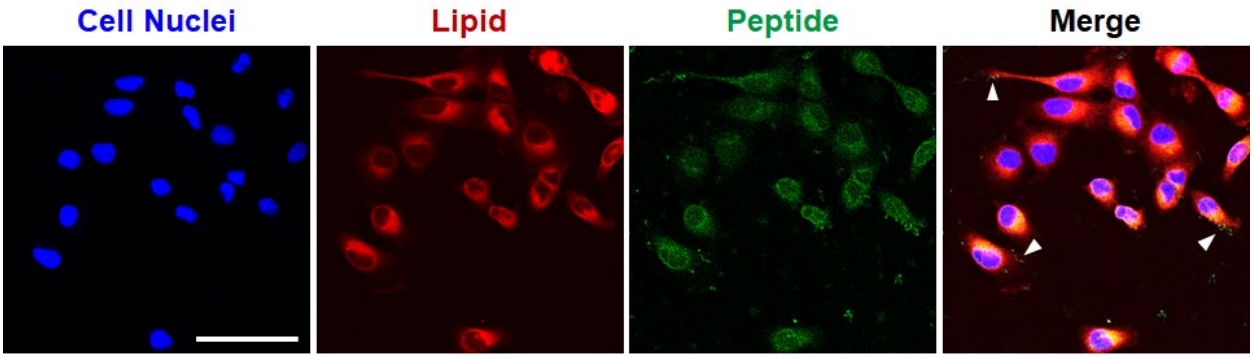

Figure 34. Fluorescent confocal microscopy images of A549 lung carcinoma cells following a 24 hour incubation with Lasioglossin-loaded LPs (scale bar = 50 μm). Lipid (red) and ACPs (green) components of the LP particles were individually labeled to track the subcellular localization of each component. White arrows in merged image highlight self-assemble ACP structures at the cancer cell membrane.

Supplemental Fig. 21. Bright field microscopy of untreated and Lasioglossin LP treated cells

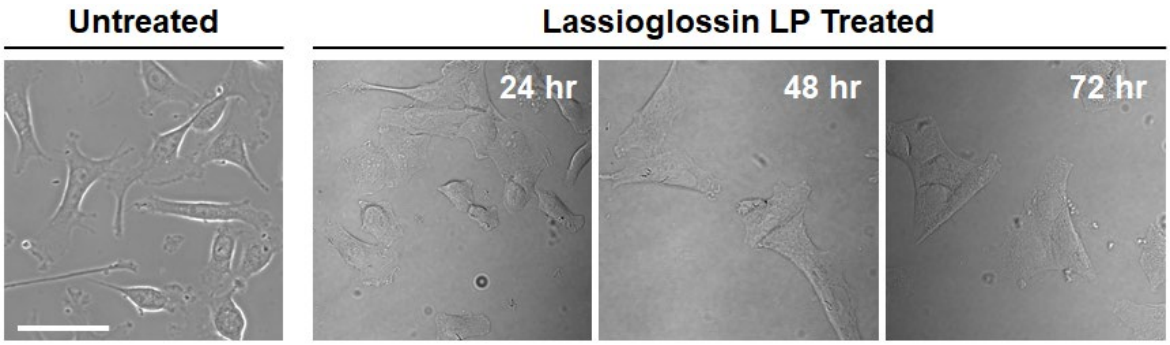

Figure 35. DIC confocal microscopy images of (Left) untreated A549 lung carcinoma cells, or (Right) those incubated for 24 - 72 hours with Lasioglossin-loaded LPs (scale bar = 50 μm).

BIBLIOGRAPHY

1. Siegel, R. L., Miller, K. D. & Jemal, A. Cancer statistics, 2019. *CA. Cancer J. Clin.* **69**, 7–34 (2019).
2. Chen, H. S. *et al.* Predicting US- and state-level cancer counts for the current calendar year: Part I: evaluation of temporal projection methods for mortality. *Cancer* (2012).
3. Zhu, L. *et al.* Predicting US- and state-level cancer counts for the current calendar year: Part II: Evaluation of spatiotemporal projection methods for incidence. *Cancer* (2012). doi:10.1002/cncr.27405
4. Pickle, L. W. *et al.* A New Method of Estimating United States and State-level Cancer Incidence Counts for the Current Calendar Year. *CA. Cancer J. Clin.* (2007). doi:10.3322/canjclin.57.1.30
5. Housman, G. *et al.* Drug resistance in cancer: An overview. *Cancers* (2014). doi:10.3390/cancers6031769
6. Mansoori, B., Mohammadi, A., Davudian, S., Shirjang, S. & Baradaran, B. The different mechanisms of cancer drug resistance: A brief review. *Advanced Pharmaceutical Bulletin* (2017). doi:10.15171/apb.2017.041
7. Gillet, J. P. & Gottesman, M. M. Mechanisms of multidrug resistance in cancer. *Methods Mol. Biol.* (2010). doi:10.1007/978-1-60761-416-6_4
8. Luqmani, Y. A. Mechanisms of Drug Resistance in Cancer Chemotherapy. *Med. Princ. Pract.* **14**, 35–48 (2005).
9. Zia, M. K. *et al.* Chemotherapeutic Drugs and Plasma Proteins: Exploring New Dimensions. *Curr. Protein Pept. Sci.* **19**, 937–947 (2018).
10. Liu, C., Liu, Z. & Wang, J. Uncovering the molecular and physiological processes of anticancer leads binding human serum albumin: A physical insight into drug efficacy. *PLoS One* **12**, e0176208 (2017).
11. Alfarouk, K. O. *et al.* Resistance to cancer chemotherapy: failure in drug response from ADME to

P-gp. *Cancer Cell Int.* **15**, 71 (2015).

12. Aronson, M. R., Simonson, A. W., Orchard, L. M., Llinás, M. & Medina, S. H. Lipopeptisomes: Anticancer peptide-assembled particles for fusolytic oncotherapy. *Acta Biomater.* **80**, 269–277 (2018).

13. Pearce, A. *et al.* Incidence and severity of self-reported chemotherapy side effects in routine care: A prospective cohort study. *PLoS One* **12**, (2017).

14. Nakamura, T. *et al.* Fas-mediated apoptosis in Adriamycin-induced cardiomyopathy in rats: In vivo study. *Circulation* **102**, 572–578 (2000).

15. Zhao, L. & Zhang, B. Doxorubicin induces cardiotoxicity through upregulation of death receptors mediated apoptosis in cardiomyocytes. *Sci. Rep.* **7**, (2017).

16. Wanderas, E. H., Fossa, S. D., Tretli, S. & Klepp, O. Toxicity in long-term survivors after adriamycin containing chemotherapy of malignant germ cell tumours. *Int. J. Oncol.* **4**, 681–688 (1994).

17. Tao, J. J., Visvanathan, K. & Wolff, A. C. Long term side effects of adjuvant chemotherapy in patients with early breast cancer. *Breast* **24**, S149–S153 (2015).

18. Chaudhary, U. B. & Haldas, J. R. Long-term complications of chemotherapy for germ cell tumours. *Drugs* **63**, 1565–1577 (2003).

19. Hatzopoulos, S., Di Stefano, M., Albertin, A. & Martini, A. Evaluation of cisplatin ototoxicity in a rat animal model. in *Annals of the New York Academy of Sciences* **884**, 211–225 (New York Academy of Sciences, 1999).

20. Gregg, R. W. *et al.* Cisplatin neurotoxicity: The relationship between dosage, time, and platinum concentration in neurologic tissues, and morphologic evidence of toxicity. *J. Clin. Oncol.* **10**, 795–803 (1992).

21. Surendiran, A. *et al.* Adverse drug reaction profile of cisplatin-based chemotherapy regimen in a tertiary care hospital in India: An evaluative study. *Indian J. Pharmacol.* **42**, 40–43 (2010).

22. Hamers, F. P. T., Gispen, W. H. & Neijt, J. P. Neurotoxic side-effects of cisplatin. in *European Journal of Cancer and Clinical Oncology* **27**, 372–376 (1991).

23. Agarwal, R. & Kaye, S. B. Ovarian cancer: strategies for overcoming resistance to chemotherapy. *Nat. Rev. Cancer* **3**, 502–516 (2003).

24. Eckstein, N. Platinum resistance in breast and ovarian cancer cell lines. *J. Exp. Clin. Cancer Res.* **30**, 91 (2011).

25. Al-Lazikani, B., Banerji, U. & Workman, P. Combinatorial drug therapy for cancer in the post-genomic era. *Nat. Biotechnol.* **30**, 679 (2012).

26. DeStefano, C. B. & Liu, S. V. Combinatorial Immunotherapy and Chemotherapy. in *Early Phase Cancer Immunotherapy* (eds. Patel, S. P. & Kurzrock, R.) 199–218 (Springer International Publishing, 2018). doi:10.1007/978-3-319-63757-0_7

27. Aina, O. H. *et al.* From combinatorial chemistry to cancer-targeting peptides. *Mol. Pharm.* **4**, 631–651 (2007).

28. Riedl, S., Zweytick, D. & Lohner, K. Membrane-active host defense peptides - Challenges and perspectives for the development of novel anticancer drugs. *Chem. Phys. Lipids* **164**, 766–781 (2011).

29. Al-Benna, S., Shai, Y., Jacobsen, F. & Steinstraesser, L. Oncolytic activities of host defense peptides. *Int. J. Mol. Sci.* **12**, 8027–8051 (2011).

30. Gaspar, D., Veiga, A. S. & Castanho, M. A. R. B. From antimicrobial to anticancer peptides. A review. *Front. Microbiol.* **4**, (2013).

31. Lawler, S. E., Speranza, M.-C., Cho, C.-F. & Chiocca, E. A. Oncolytic viruses in cancer treatment: a review. *JAMA Oncol.* **3**, 841–849 (2017).

32. Tyagi, A. *et al.* In silico models for designing and discovering novel anticancer peptides. *Sci. Rep.* **3**, 2984 (2013).

33. Thundimadathil, J. Cancer treatment using peptides: current therapies and future prospects. *J. Amino*

Acids **2012**, (2012).

34. Zhao, J., Huang, Y., Liu, D. & Chen, Y. Two hits are better than one: synergistic anticancer activity of α-helical peptides and doxorubicin/epirubicin. *Oncotarget* **6**, 1769 (2015).

35. Felício, M. R., Silva, O. N., Gonçalves, S., Santos, N. C. & Franco, O. L. Peptides with Dual Antimicrobial and Anticancer Activities. *Front. Chem.* **5**, 5 (2017).

36. Gabernet, G., Müller, A. T., Hiss, J. A. & Schneider, G. Membranolytic anticancer peptides. *Med. Chem. Commun.* **7**, 2232–2245 (2016).

37. Camilio, K. A. Short Lytic Anticancer Peptides as a Novel Therapy against Cancer. (University of Tromsø, 2013).

38. Papo, N. & Shai, Y. Host defense peptides as new weapons in cancer treatment. *Cellular and Molecular Life Sciences* **62**, 784–790 (2005).

39. Avci, F. G., Akbulut, B. S. & Ozkirimli, E. Membrane active peptides and their biophysical characterization. *Biomolecules* **8**, (2018).

40. Schweizer, F. Cationic amphiphilic peptides with cancer-selective toxicity. *Eur. J. Pharmacol.* **625**, 190–194 (2009).

41. Shai, Y. Mechanism of the binding, insertion and destabilization of phospholipid bilayer membranes by α-helical antimicrobial and cell non-selective membrane-lytic peptides. *Biochimica et Biophysica Acta - Biomembranes* **1462**, 55–70 (1999).

42. Bertelsen, K. *et al.* Mechanisms of Peptide-Induced Pore Formation in Lipid Bilayers Investigated by Oriented 31 P Solid-State NMR Spectroscopy. (2012). doi:10.1371/journal.pone.0047745

43. Zeth, K. & Sancho-Vaello, E. The Human Antimicrobial Peptides Dermcidin and LL-37 Show Novel Distinct Pathways in Membrane Interactions. *Front. Chem.* **5**, (2017).

44. Gajski, G. & Garaj-Vrhovac, V. Melittin: a lytic peptide with anticancer properties. *Environ. Toxicol. Pharmacol.* **36**, 697–705 (2013).

45. Suarez-Jimenez, G.-M., Burgos-Hernandez, A. & Ezquerra-Brauer, J.-M. Bioactive peptides and

depsipeptides with anticancer potential: Sources from marine animals. *Mar. Drugs* **10**, 963–986 (2012).

46. Zheng, L.-H. *et al.* Antitumor peptides from marine organisms. *Mar. Drugs* **9**, 1840–1859 (2011).

47. Seo, M.-D., Won, H.-S., Kim, J.-H., Mishig-Ochir, T. & Lee, B.-J. Antimicrobial peptides for therapeutic applications: a review. *Molecules* **17**, 12276–12286 (2012).

48. Kościuczuk, E. M. *et al.* Cathelicidins: family of antimicrobial peptides. A review. *Mol. Biol. Rep.* **39**, 10957–10970 (2012).

49. Kumar, P., Kizhakkedathu, J. N. & Straus, S. K. Antimicrobial peptides: Diversity, mechanism of action and strategies to improve the activity and biocompatibility in vivo. *Biomolecules* **8**, 4 (2018).

50. Bahar, A. A. & Ren, D. Antimicrobial peptides. *Pharmaceuticals* **6**, 1543–1575 (2013).

51. Fuster, M. M. & Esko, J. D. The sweet and sour of cancer: glycans as novel therapeutic targets. *Nat. Rev. Cancer* **5**, 526–542 (2005).

52. Ishikawa, K., Medina, S. H., Schneider, J. P. & Klar, A. J. S. S. Glycan Alteration Imparts Cellular Resistance to a Membrane-Lytic Anticancer Peptide. *Cell Chem. Biol.* **24**, 149–158 (2017).

53. Medina, S. H. & Schneider, J. P. Cancer cell surface induced peptide folding allows intracellular translocation of drug. *J. Control. Release* **209**, 317–326 (2015).

54. Sharma, B. & Kanwar, S. S. Phosphatidylserine: A cancer cell targeting biomarker. *Semin. Cancer Biol.* **52**, 17–25 (2018).

55. Deslouches, B. & Peter Di, Y. Antimicrobial peptides with selective antitumor mechanisms: Prospect for anticancer applications. *Oncotarget* **8**, 46635–46651 (2017).

56. Van Meer, G., Voelker, D. R. & Feigenson, G. W. Membrane lipids: Where they are and how they behave. *Nature Reviews Molecular Cell Biology* **9**, 112–124 (2008).

57. Ingólfsson, H. I. *et al.* Lipid organization of the plasma membrane. *J. Am. Chem. Soc.* **136**, 14554–14559 (2014).

58. Mohandas, N. & Gallagher, P. G. Red cell membrane: Past, present, and future. *Blood* **112**, 3939–

3948 (2008).

59. Balasubramanian, K. & Schroit, A. J. Aminophospholipid Asymmetry: A Matter of Life and Death. *Annu. Rev. Physiol.* **65**, 701–734 (2003).

60. Chaurio, R. A. *et al.* Phospholipids: Key players in apoptosis and immune regulation. *Molecules* **14**, 4892–4914 (2009).

61. Zwaal, R. F. A., Comfurius, P. & Bevers, E. M. Surface exposure of phosphatidylserine in pathological cells. *Cell. Mol. Life Sci.* **62**, 971–988 (2005).

62. Doyle, J. *et al.* nNOS inhibition, antimicrobial and anticancer activity of the amphibian skin peptide, citropin 1.1 and synthetic modifications. The solution structure of a modified citropin 1.1. *Eur. J. Biochem.* **270**, 1141–1153 (2003).

63. Slaninová, J. *et al.* Toxicity study of antimicrobial peptides from wild bee venom and their analogs toward mammalian normal and cancer cells. *Peptides* **33**, 18–26 (2012).

64. Friedman, M. Applications of the Ninhydrin Reaction for Analysis of Amino Acids, Peptides, and Proteins to Agricultural and Biomedical Sciences. *J. Agric. Food Chem.* **52**, 385–406 (2004).

65. Medina, S. H. *et al.* An Intrinsically Disordered Peptide Facilitates Non-Endosomal Cell Entry. *Angew. Chemie* **55**, 3369–3372 (2016).

66. Sinthuvanich, C. *et al.* Anticancer β-hairpin peptides: Membrane-induced folding triggers activity. *J. Am. Chem. Soc.* **134**, 6210–6217 (2012).

67. Uphoff, C. C. & Drexler, H. G. Detection of Mycoplasma Contaminations. in *Basic Cell Culture Protocols* (eds. Helgason, C. D. & Miller, C. L.) 13–23 (Humana Press, 2005). doi:10.1385/1-59259-838-2:013

68. Simonson, A. W., Lawanprasert, A., Goralski, T. D. P., Keiler, K. C. & Medina, S. H. Bioresponsive peptide-polysaccharide nanogels — A versatile delivery system to augment the utility of bioactive cargo. *Nanomedicine* **17**, 391–400 (2019).

69. Simonson, A. W. *et al.* Pathogen-specific de novo antimicrobials engineered through membrane

porin biomimicry. *Under Rev.* (2020).

70. Reißer, S., Strandberg, E., Steinbrecher, T. & Ulrich, A. S. 3D hydrophobic moment vectors as a tool to characterize the surface polarity of amphiphilic peptides. *Biophys. J.* **106**, 2385–2394 (2014).

71. Teixeira, V., Feio, M. J. & Bastos, M. Role of lipids in the interaction of antimicrobial peptides with membranes. *Prog. Lipid Res.* **51**, 149–177 (2012).

72. Cochran, A. G., Skelton, N. J. & Starovasnik, M. A. Tryptophan zippers: Stable, monomeric β-hairpins. *Proc. Natl. Acad. Sci.* **98**, 5578–5583 (2001).

73. Rivel, T., Ramseyer, C. & Yesylevskyy, S. The asymmetry of plasma membranes and their cholesterol content influence the uptake of cisplatin. *Sci. Rep.* **9**, 1–14 (2019).

74. Manzo, G. *et al.* Enhanced amphiphilic profile of a short β-stranded peptide improves its antimicrobial activity. *PLoS One* **10**, 1–18 (2015).

75. Andrushchenko, V. V., Vogel, H. J. & Prenner, E. J. Solvent-dependent structure of two tryptophan-rich antimicrobial peptides and their analogs studied by FTIR and CD spectroscopy. *Biochim. Biophys. Acta - Biomembr.* (2006). doi:10.1016/j.bbamem.2006.07.013

76. Chen, W., Ding, H., Feng, P., Lin, H. & Chou, K.-C. iACP: a sequence-based tool for identifying anticancer peptides. *Oncotarget* **7**, 16895 (2016).

77. Huang, Y., Wang, X., Wang, H., Liu, Y. & Chen, Y. Studies on mechanism of action of anticancer peptides by modulation of hydrophobicity within a defined structural framework. *Mol. Cancer Ther.* **10**, 416–426 (2011).

78. Tyson, R. A., Zatulovskiy, E., Kay, R. R. & Bretschneider, T. How blebs and pseudopods cooperate during chemotaxis. *Proc. Natl. Acad. Sci.* **111**, 11703–11708 (2014).

79. Drin, G. & Antonny, B. Amphipathic helices and membrane curvature. *FEBS Lett.* **584**, 1840–1847 (2010).

80. Gómez-Llobregat, J., Elías-Wolff, F. & Lindén, M. Anisotropic membrane curvature sensing by amphipathic peptides. *Biophys. J.* **110**, 197–204 (2016).

81. Mészáros, N. *et al.* Nuclear Pore Basket Proteins Are Tethered to the Nuclear Envelope and Can Regulate Membrane Curvature. *Dev. Cell* **33**, 285–298 (2015).

82. Ashkenazi, A. Targeting the extrinsic apoptosis pathway in cancer. *Cytokine Growth Factor Rev.* **19**, 325–331 (2008).

83. Emelianova, A. A. *et al.* Anticancer activity of the goat antimicrobial peptide ChMAP-28. *Front. Pharmacol.* **9**, 1501 (2018).

84. Hou, L. *et al.* Antitumor activity of antimicrobial peptides containing CisoDGRC in CD13 negative breast cancer cells. *PLoS One* **8**, (2013).

85. Kim, I.-W. *et al.* Anticancer activity of a synthetic peptide derived from harmoniasin, an antibacterial peptide from the ladybug Harmonia axyridis. *Int. J. Oncol.* **43**, 622–628 (2013).

86. Kuroda, K. *et al.* Antimicrobial peptide FF/CAP18 induces apoptotic cell death in HCT116 colon cancer cells via changes in the metabolic profile. *Int. J. Oncol.* **46**, 1516–1526 (2015).

87. Ahmed, N. & Stenvers, K. Getting to know ovarian cancer ascites: opportunities for targeted therapy-based translational research. *Front. Oncol.* **3**, 256 (2013).

88. Fernandez, D. I., Gehman, J. D. & Separovic, F. Membrane interactions of antimicrobial peptides from Australian frogs. *Biochim. Biophys. Acta - Biomembr.* (2009). doi:10.1016/j.bbamem.2008.10.007

89. Čeřovský, V. *et al.* Lasioglossins: Three novel antimicrobial peptides from the venom of the eusocial bee Lasioglossum laticeps (hymenoptera: halictidae). *ChemBioChem* (2009). doi:10.1002/cbic.200900133

90. Leuschner, C. & Hansel, W. Membrane Disrupting Lytic Peptides for Cancer Treatments. *Curr. Pharm. Des.* **10**, 2299–2310 (2005).

91. Gaspar, D., Veiga, A. S., Sinthuvanich, C., Schneider, J. P. & Castanho, M. A. R. B. Anticancer peptide SVS-1: Efficacy precedes membrane neutralization. *Biochemistry* (2012). doi:10.1021/bi300836r

92. Wang, C. *et al.* Melanoma cell surface-expressed phosphatidylserine as a therapeutic target for cationic anticancer peptide, temporin-1CEa. *J. Drug Target.* (2016). doi:10.3109/1061186X.2015.1113539

93. Baeza-Delgado, C., Von Heijne, G., Marti-Renom, M. A. & Mingarro, I. Biological insertion of computationally designed short transmembrane segments. *Sci. Rep.* (2016). doi:10.1038/srep23397

94. Kučerka, N., Kiselev, M. A. & Balgavý, P. Determination of bilayer thickness and lipid surface area in unilamellar dimyristoylphosphatidylcholine vesicles from small-angle neutron scattering curves: A comparison of evaluation methods. *Eur. Biophys. J.* (2004). doi:10.1007/s00249-003-0349-0

95. Monincová, L. *et al.* Novel antimicrobial peptides from the venom of the eusocial bee Halictus sexcinctus (Hymenoptera: Halictidae) and their analogs. *Amino Acids* (2010). doi:10.1007/s00726-010-0519-1

96. Düzgünes, N., Wilschut, J., Fraley, R. & Papahadjopoulos, D. Studies on the mechanism of membrane fusion. Role of head-group composition in calcium- and magnesium-induced fusion of mixed phospholipid vesicles. *BBA - Biomembr.* (1981). doi:10.1016/0005-2736(81)90148-6

97. Hay, J. C. Calcium: A fundamental regulator of intracellular membrane fusion? *EMBO Reports* (2007). doi:10.1038/sj.embor.7400921

98. Currie, E., Schulze, A., Zechner, R., Walther, T. C. & Farese, R. V. Cellular fatty acid metabolism and cancer. *Cell Metabolism* (2013). doi:10.1016/j.cmet.2013.05.017

99. Beloribi-Djefaflia, S., Vasseur, S. & Guillaumond, F. Lipid metabolic reprogramming in cancer cells. *Oncogenesis* (2016). doi:10.1038/oncsis.2015.49

100. Huang, Y. B., He, L. Y., Jiang, H. Y. & Chen, Y. X. Role of helicity on the anticancer mechanism of action of cationic-helical peptides. *Int. J. Mol. Sci.* (2012). doi:10.3390/ijms13066849

101. Alnaim, L. Therapeutic drug monitoring of cancer chemotherapy. *Journal of Oncology Pharmacy Practice* (2007). doi:10.1177/1078155207081133

102. Steck, T. L. The organization of proteins in the human red blood cell membrane: A review. *J. Cell*

Biol. (1974). doi:10.1083/jcb.62.1.1

103. Zwaal, R. F. A. & Schroit, A. J. Pathophysiologic implications of membrane phospholipid asymmetry in blood cells. *Blood* (1997). doi:10.1182/blood.v89.4.1121

104. Paci, A. *et al.* Review of therapeutic drug monitoring of anticancer drugs part 1 - Cytotoxics. *European Journal of Cancer* (2014). doi:10.1016/j.ejca.2014.04.014

105. Begg, E. J., Barclay, M. L. & Kirkpatrick, C. J. M. The therapeutic monitoring of antimicrobial agents. *Br. J. Clin. Pharmacol.* (1999). doi:10.1046/j.1365-2125.1999.00850.x

106. Allen, T. M. & Cullis, P. R. Liposomal drug delivery systems: From concept to clinical applications. *Advanced Drug Delivery Reviews* (2013). doi:10.1016/j.addr.2012.09.037

ACADEMIC VITA

Objective

Pursue a PhD in Biomedical Engineering at a world-class research institution with well-established faculty in a laboratory that focuses on integrating principles of biomimetic materials, therapeutic design, and drug delivery to address cancer and inflammatory diseases.

Education

The Pennsylvania State University – Schreyer Honors College University Park, PA
Candidate for BS in Biomedical Engineering with Honors | Biochemical Option *Aug 2016 – present*
Relevant Courses: Organic Chemistry I/II, Biomedical Materials, Biopolymers, Fundamentals of Biochemistry

The National University of Singapore – University Scholars Program Singapore
Faculty of Engineering | Study Abroad Exchange Program *Spring Semester 2018*

Research Experience

Undergraduate Research Assistant University Park, PA
Precision Therapeutics and Bioresponsive Materials Lab – Penn State University *Feb 2017 – present*

- Synthesized designed peptides and analytically characterized products with HPLC-MS and circular dichroism
- Engineered liposomes for model membrane studies and anticancer lipopeptisome design via freeze/thaw and extrusion
- Conducted MTT cell viability assays and confocal microscopy on mammalian cells
- Experimented with biophysical characterization with dynamic light scattering, SEM, and UV-VIS
- Completed data analysis with Microsoft Excel, GraphPad Prism, and MATLAB

DAAD RISE Research Fellow Kaiserslautern, Germany
Lehrgebiet Bioverfahrenstechnik (BioVT) – Technische Universität Kaiserslautern *June – Aug 2019*

- Isolated antimicrobial molecules from terrestrial cyanobacteria using liquid/solid extraction protocols
- Developed purification methods on fPLC and analyzed extractions via HPLC-MS and NMR
- Conducted resazurin assays for bacterial inhibition studies with extracted bioactive compounds

Undergraduate Research Assistant Philadelphia, PA
Jonathan Soboloff Research Group – Fels Institute for Cancer Research and Molecular Biology *June – Sept 2018*

- Experimented with primary human cell lines and human mesenchymal stem cells
- Performed calcium quantification across cell membranes with epifluorescent and confocal microscopy

Publications

1. **Matthew R. Aronson**, Erika S. Dahl, Jacob A. Halle, Rose A. Gogal, Andrew W. Simonson, Adam B. Glick, Katherine M. Aird, Scott H. Medina. Re-engineering antimicrobial peptides into oncolytics targeting drug-resistant ovarian cancers. *Under revision*.
2. Andrew W. Simonson, Agustey S. Mongia, **Matthew R. Aronson**, John Alumasa, Dennis C. Chan, Adam Bolotsky, Aida Ebrahimi, Elizabeth A. Proctor, Kenneth C. Keiler, Scott H. Medina. Pathogen-specific de novo antimicrobials engineered through membrane porin biomimicry. *Under Review*.
3. Atip Lawanprasert, Caitlin A. Guinan, Erica S. Langford, Carly E. Hawkins, Janna N. Sloand, Howard W. Fescemyer, **Matthew R. Aronson**, Jacob A. Halle, James H. Marden, and Scott H. Medina (2020). Discovery of antitumor lectins from rainforest tree root transcriptomes. *PLoS One, 15*(2), e0229467.
4. Go CK, Hooper R, **Aronson MR**, Schultz B, Cangoz T, Nemani N, Zhang Y, Madesh M, Soboloff J (2019). PMCA clears near-membrane Ca2+ to facilitate store-operated Ca2+ entry and NFAT activation. *Sci Signal*, **12**, eaaw2627.
5. **Aronson, M. R.**, Simonson, A. W., Orchard, L. M., Llinás, M., & Medina, S. H. (2018). Lipopeptisomes: Anticancer peptide-assembled particles for fusolytic oncotherapy. *Acta Biomaterialia*, *80*, 269-277.

Awards and Honors

- CSL Behring Senior Scholarship (2020)
- Global Engineering Fellowship Scholarship (2018, 2019, 2020)
- W. Gordon Dunning Medical Scholarship (2016, 2017, 2018, 2019, 2020)
- Schreyer Honors College Academic Excellence Scholarship (2016, 2017, 2018, 2019, 2020)
- College of Engineering Research Scholarship (2019)
- Patrick Couvreur Student Travel Award from the Controlled Release Society (2019)
- DAAD German Academic Exchange Service RISE Fellowship (2019)
- Undergraduate International Conference Travel Grant (2019)
- Schreyer Honors College Internship Grant (2019)

- Undergraduate Domestic Conference Travel Grant (2018)
- Schreyer Honors College International Study Grant (2018)
- The Pennsylvania State University Engineering Travel Grant (2018)
- Student Engagement Network Grant for Independent Research (2017)
- Schreyer Honors College Independent Research Grant (2017)

Presentations

- Poster Presentation at Penn State Cancer Institute's Cancer Research Day in University Park, PA (Nov 2019)
- Poster Presentation at Biomedical Engineering Society Annual Meeting in Philadelphia, PA (Oct 2019)
- Poster Presentation at the Controlled Release Society Annual Meeting & Exposition in Valencia, Spain (Jul 2019)
- Poster Presentation at Penn State Undergraduate Exhibition in University Park, PA (Apr 2019)
- Poster Presentation at Penn State College of Engineering Research Symposium in University Park, PA (Apr 2019)
- Oral Presentation at Biomedical Engineering Society Annual Meeting in Atlanta, GA (Oct 2018)
- Poster Presentation at Materials Day in University Park, PA (Oct 2018)
- Poster Presentation at Student Engagement Network in University Park, PA (Nov 2017, Oct 2018)

Skills and Abilities

Computer Software

- MATLAB, COMSOL, GraphPad Prism, Microsoft Excel/PowerPoint

Analytical Characterization Techniques

- LC-MS, UV-VIS, Epifluorescent Microscopy, Confocal Microscopy, Transmission Electron Microscopy, Scanning Electron Microscopy, Flow Cytometry

Analytical Separation Techniques

- HPLC-Preparative, fPLC, IC, Affinity Chromatography

Educational Enrichment

Global Engineering Fellow University Park, PA

Fellow *Aug 2018 – present*

- Improve communication, professional development, and intercultural skills by sharing personal study abroad experiences through participation in an academic program/course focused on global, professional development
- Run events, activities, and work with guest speakers
- Hold office hours to assist other undergraduate students pursue their desire to study abroad

Extracurricular

Biomedical Engineering Society – Penn State Chapter University Park, PA

Volunteer Chair (2016 – 2017), Fundraising Chair (2017 – 2018) *Aug 2016 – present*

- Provides resources on a local and global scale for the pursuit of scholarly activities and intellectual growth
- Encourages opportunities for networking and collaboration among students, faculty, and companies
- Improve communication, professional development, and intercultural skills by sharing personal study abroad experiences by participating in an academic program/course focused on global, professional development
- Run events/activities, work with guest speakers, and hold office hours to assist students wishing to study abroad

BKind at Penn State University Park, PA

Funds Director *Aug 2018 – May 2019*

- BKind provides ways for students to spread kindness on campus and track their good deeds
- Organize community service events, specifically the financial aspects

Community Service

Newtown Ambulance Squad Newtown, PA

Senior 911 BLS Care Provider – Volunteer Emergency Medical Technician (EMT) *Jan 2014 – present*

- Work with EMTs and Paramedics with the evaluation and treatment of patients
- Conduct continuing education courses in-person and online on relevant material

Young Chefs, Inc. Newtown, PA

Founder and President *Mar 2012 – present*

- Established nonprofit organization to prepare and deliver homemade meals to women undergoing breast cancer treatment
- Networked with local food store, McCaffrey's Markets, to donate all ingredients
- Received referrals through our website, www.youngchefsbc.org, local hospitals, and support groups